Development and evaluation of an advanced National Air Quality Forecast Capability using the NOAA Global Forecast System version 16

Patrick C. Campbell[1,2,*], Youhua Tang[1,2], Pius Lee[1], Barry Baker[1], Daniel Tong[1,2], Rick Saylor[1], Ariel Stein[1], Jianping Huang[3,4], Ho-Chun Huang[3,4], Edward Strobach[3,4], Jeff McQueen[3], Li Pan[3,4], Ivanka Stajner[3], Jamese Sims[5], Jose Tirado-Delgado[5,6], and Youngsun Jung[5], Fanglin Yang[3], Tanya L. Spero[7], and Robert C. Gilliam[7]

1. NOAA Air Resources Laboratory (ARL), College Park, MD, USA.
2. Center for Spatial Information Science and Systems, George Mason University, Fairfax, VA., USA.
3. NOAA National Centers for Environmental Prediction (NCEP), College Park, MD, USA.
4. I.M. Systems Group Inc., Rockville, MD, USA.
5. NOAA NWS/STI, USA.
6. Eastern Research Group, Inc (ERG), USA.
7. U.S. Environmental Protection Agency, Research Triangle Park, NC, USA.

*Corresponding Author: Patrick.C.Campbell@noaa.gov

Abstract

A new dynamical core, known as the Finite Volume Cubed-Sphere (FV3) and developed at both NASA and NOAA, is used in NOAA's Global Forecast System (GFS) and in limited area models (LAMs) for regional weather and air quality applications. NOAA has also upgraded the operational FV3GFS to version 16 (GFSv16), and includes a number of significant developmental advances to the model configuration, data assimilation, and underlying model physics, particularly for atmospheric composition to weather feedback. Concurrent with the GFSv16 upgrade, we couple the GFSv16 with the Community Multiscale Air Quality (CMAQ) model to form an advanced version of the National Air Quality Forecast Capability (NAQFC) that will continue to protect human and ecosystem health in the U.S. Here we describe the development of the FV3GFSv16 coupling with a "state-of-the-science" CMAQ model version 5.3.1. The GFS-CMAQ coupling is made possible by the seminal version of the NOAA-ARL Atmosphere-Chemistry Coupler

35 (NACC), which became the next operational NAQFC system (i.e., NACC-CMAQ) on July

36 20, 2021. NACC-CMAQ has a number of scientific advancements that include satellite-

37 based data acquisition technology to improve land cover and soil characteristics, and inline

38 wildfire smoke and dust predictions that are vital to predictions of fine particulate matter

39 ($PM_{2.5}$) concentrations during hazardous events affecting society, ecosystems, and human

40 health. The GFS-driven NACC-CMAQ has significantly different meteorological and

41 chemical predictions than the previous operational NAQFC, where evaluation of NACC-

42 CMAQ shows generally improved near-surface ozone and $PM_{2.5}$ predictions and diurnal

43 patterns, both of which are extended to a 72-hour (3-day) forecast with this system.

1. Introduction

Air quality is defined as the degree in which the ambient air is free of pollutants--which are either directly emitted into the atmosphere (primary air pollutants) or formed within the atmosphere itself (secondary air pollutants)--that cause degradation to human health, visibility, and/or ecological systems (WHO, 2005). Air quality is as ubiquitous and important as weather impacts, where outdoor air pollution is responsible for ~4.2 million early deaths globally each year (https://www.who.int/health-topics/air-pollution#tab=tab_1). To put this into perspective: this is over three times the number of people who die from HIV/AIDS and over eight times the number of homicides each year (2017 Global Burden of Disease Study: https://www.thelancet.com/gbd). Air pollution is costly, and leads to huge economic damage (Landrigan et al., 2018). There are also disproportionate impacts of air pollution across poorer people and some racial and ethnic groups, who are among those who often face higher exposure and potential responses to pollutants (Institute of Medicine, 1999; American Lung Association, 2001; O'Neil et al., 2003; Finkelstein et al., 2003; Zeka et al., 2006).

Air pollutants are composed of both gaseous and particulate species, which under prolonged exposure can cause non-carcinogenic (Lee et al., 2014) and/or carcinogenic adverse health effects (Demetirou and Vineis, 2015). High ground-level ozone (O_3) concentrations (i.e., smog) for example, can lead to decreased lung function and cause respiratory symptoms. These symptoms are particularly dangerous for sensitive groups such as young children, the elderly, and those with preexisting conditions that include asthma, chronic obstructive pulmonary disease (COPD), lung cancer, and respiratory infection (Kar Kurt et al., 2016).

To protect against the health and environmental impacts of air pollution, world agencies have developed regulations and standards on the allowable amount of primary and secondary air

82   pollution measured at different spatiotemporal scales (e.g., seconds to months and local to global

83   scales), which largely depend on the atmospheric lifetime of specific air components (WHO,

84   2005, 2010). Typically, the world's most extreme air pollution occurs near global megacities

85   where population density is highest (Marlier et al., 2016). Rapid economic growth in China, for

86   example has led to extremely high air pollution levels over the past decade (Zhou et al., 2017;

87   Liu and Wang, 2020), necessitating significant efforts to implement air pollution prevention and

88   control plans (Chinese State Council, 2013; Zhao et al., 2014). The U.S. Environmental

89   Protection Agency (EPA) defines ambient concentration limits for primary pollutants such as

90   sulfur dioxide (SO_2), oxides of nitrogen ($NO_x = NO+NO_2$), carbon monoxide (CO), lead (Pb),

91   and total (carbonaceous and non-carbonaceous) particulate matter (PM). Other important

92   primary pollutants include total volatile organic compounds (VOCs), which have many sources

93   (both natural and anthropogenic) and serve as vital precursor gases to secondary pollutants such

94   as ground-level O_3 and the formation of fine particulate matter with an aerodynamic diameter of

95   less than 2.5 μm ($PM_{2.5}$). Ground level O_3 and $PM_{2.5}$ are two of the six U.S. EPA "criteria

96   pollutants" that are regulated for their concentrations, exposure level, and health impacts. This is

97   largely because there is a relatively mature understanding of their sources, formation, and

98   characteristics (e.g., Sillman et al., 1990; Sillman 1995, 1999; Pinder et al., 2008; Kim et al.,

99   2011a, 2011b; Zhang et al., 2009a, 2009b; Campbell et al., 2015; Karamchandani, et al. 2017).

100   There is also a widespread ability to compare observed and simulated ambient ozone

101   concentrations over both short-term (McKeen et al., 2004, 2007, 2009) and dynamic long-term

102   periods (e.g., Astitha et al., 2017), which has helped lead to an understanding of their well-

103   attributable health impacts (e.g., WHO 2006, Sun et al., 2015; Zhang et al., 2018).

104   To address prolific air pollution concerns in the U.S. during the 1950s-1960s, the first

105   development and application of real-time air quality forecast (RT-AQF) models began in the

106   1970s-1980s (i.e., the 1st and 2nd generation air quality models) coincident with the

107   establishment of the U.S. EPA by President Nixon. Initially the models were based on empirical

108   approaches and statistical models (Zhang et al., 2012a); however, by the 1990s and early 2000s,

109   RT-AQF models underwent a significant evolution and evolved to more complex 3-D numerical

110   air quality models (3rd and 4th generation air quality models). These RT-AQF models involved

111   more sophisticated techniques including increasingly complex parameterizations and chemistry,

112   bias correction methods and data fusion, chemical data assimilation, and hybrid statistical or

113   numerical methods with artificial intelligence/machine learning algorithms to improve RT-AQF

114   model efficiency and predictions (Zhang et al., 2012b; Bai et al., 2018). RT-AQF models have

115   become vital tools to improve our understanding and prediction of how air pollutants form,

116   disperse, and deposit to the surface, and are used by local health and air managers to assess the

117   air quality conditions to make informed decisions on mitigation measures to reduce public

118   exposure.

119   To address the nation's need for reducing the adverse health effects of air pollution and

120   associated costly medical expenses, in 2002 Congress addressed the National Oceanic and

121   Atmospheric Administration (NOAA) to provide National AQF guidance (H.R. Energy Policy

122   Act of 2002 - Senate Amendment S. 517, SA1383, Forecasts and Warnings). A joint project

123   emerged from this amendment between NOAA and the EPA to develop and establish the initial

124   phase of a RT-AQF system, which consisted of the coupled NOAA's Eta meteorological model

125   (Black, 1994; Rogers et al., 1996) with EPA's Models-3 Community Multiscale Air Quality

126   (CMAQ) model (Byun and Ching, 1999; Byun and Schere, 2006). This "offline-coupled" model

127 provided O_3 forecast guidance for the northeastern U.S states (Kang et al., 2005; Otte et al.,

128 2005; Eder et al., 2006) and formed the early version of the National Air Quality Forecast

129 Capability (NAQFC) that was first implemented for operations in September 2004

130 (https://www.weather.gov/sti/stimodeling_airquality_predictions).   The NAQFC was further

131 developed at NOAA and collaborating laboratories (Mathur et al., 2008; McKeen et al., 2004,

132 2007, 2009), and was comprehensively evaluated in Eder et al. (2009). The NAQFC has been

133 continuously advanced to provide both O_3 and $PM_{2.5}$ forecast guidance for the entire

134 conterminous U.S. (CONUS), expanded its predictions to both Alaska and Hawaii, and provided

135 pivotal air quality forecast guidance to a multitude of stakeholders to help protect human health

136 and the environment (Stajner et al., 2011; Lee et al., 2017; Huang et al., 2017). Prior to the

137 advanced version described in this paper, the NAQFC used the offline-coupled North American

138 Mesoscale Model Forecast System on the B-Grid (NMMB) (Black, 1994; Janjic and Gall, 2012)

139 and CMAQv5.0.2 (U.S. EPA, 2014). The NAQFC provides forecast guidance for O_3, $PM_{2.5}$,

140 wildfire smoke, and dust at a horizontal grid spacing of 12 km over a domain centered on the

141 CONUS, Alaska, and Hawaii domains.

142   NOAA's National Weather Service (NWS) transitioned operationally in June 2019 to use a

143 new dynamical core known as the Finite Volume Cubed-Sphere (FV3) in the Global Forecast

144 System (GFS) model. Both the National Aeronautics and Space Administration (NASA) and

145 NOAA's Geophysical Fluid Dynamics Laboratory (GFDL; https://www.gfdl.noaa.gov/) have

146 developed and advanced FV3 over the past few decades (Lin et al., 1994; Lin and Rood, 1996;

147 Lin, 2004; Putman and Lin, 2007; Chen et al., 2013; Harris and Lin, 2013; Harris et al., 2016;

148 Zhou et al., 2019).   Overall, the switch to a FV3-based dynamical core with advancements to

149 GFS's observation quality control, data assimilation, and model physical parameterizations (from

150   the National Center for Environmental Prediction) significantly increases the accuracy of 1-2 day

151   and longer (e.g., 3-7 day) weather forecasts (Chen et al., 2018). Other advantages of FV3GFS

152   are improved computational efficiency and adaptable scaling, enhanced and flexible vertical

153   resolution, and improved representation of atmospheric circulation and weather patterns across

154   different horizontal scales (Yang et al., 2020;

155   https://www.weather.gov/media/notification/pns20-44gfs_v16.pdf;

156   https://www.emc.ncep.noaa.gov/emc/pages/numerical_forecast_systems/gfs.php;

157   https://ufscommunity.org/wp-

158   content/uploads/2020/10/UFS_Webnair_GFSv16_20201022_FanglinYang.pdf).

159   The improved representation of atmospheric conditions, circulation/transport, and

160   precipitation in GFS are pivotal to the accuracy of chemical predictions when coupled to RT-

161   AQF models. Since 2017, there also has been significant efforts at NOAA to use version 15 of

162   FV3GFS (hereafter, GFSv15) rather than NMMB as the meteorological driver for CMAQ in the

163   NAQFC (Huang et al., 2018, 2019, 2020). Huang et al. (2020) and Chen et al. (2021)

164   demonstrated that a version of the GFS-driven CMAQv5.0.2 (GFSv15-CMAQ) forecasting

165   system had improved O_3 predictions compared to the NMMB-driven CMAQ (NMMB-CMAQ)

166   system, but that the GFSv15-CMAQ had large biases for $PM_{2.5}$ that still need improvement.

167   Concurrently at NOAA, there is a major upgrade of GFS from version 15 to 16 (GFSv16),

168   which includes a number of major developmental advances to the system (see Section 2 of this

169   paper). Thus, there was an opportunity to simultaneously upgrade and streamline the

170   meteorological coupling between the GFSv16 and a more updated, "state-of-the-science" version

171   of CMAQ at the U.S. EPA (U.S. EPA, 2019; Appel et al., 2021). The current CMAQv5.0.2 used

172   in the NMMB-CMAQ and experimental GFSv15-CMAQ is outdated scientifically with

173   numerous deficiencies, many of which led to the elevated biases and error as described in Huang

174   et al. (2017; 2020) and Chen et al. (2021). Hence, there is a need to update the NAQFC to

175   actively developing versions of both FV3GFS and CMAQ.

176   The main objectives of this manuscript are to describe the development of the GFSv16

177   coupling with a state-of-the-science CMAQ model for the advanced updates to NAQFC that

178   includes numerous other RT-AQF science advances (Section 2). We also describe the new

179   simulation design and input observations, and evaluate the meteorological and air quality

180   predictions across the U.S. compared to the now discontinued NMMB-CMAQ system for

181   NAQFC (Sections 3 and 4). We conclude with a summary of NACC-CMAQ serving as the

182   current (since July 20, 2021) operational NAQFC, as well as longer-term goals (Section 5). We

183   hypothesize that advancing to closer state-of-the-science meteorological and chemical transport

184   models will improve atmospheric-chemical composition predictions, and the resulting air quality

185   forecasts will better protect human health across the U.S.

186   **2.   Methods**
187
188   2.1 Updated Meteorological and Surface Drivers
189
190   *2.1.1 The Global Forecast System Version 16*
191
192   The Environmental Modeling Center (EMC) at NOAA continuously develops and

193   improves the GFS model, which has been in operation at the National Weather Service since

194   1980. EMC has recently upgraded the GFS model from v15.3 to v16 in February 2021, and the

195   major upgrade improves the model forecast performance while also providing enhanced forecast

196   products. Some of the major structural changes to GFSv16 (compared to previous GFS versions)

197   include increased vertical layers/resolution from 64 to 127 (Figure 1) and an extended model top

198   from 54 (upper stratosphere) to 80 km (mesopause). GFSv16 also has a thinner first model layer

199   thickness (20 m) and higher resolution global horizontal grids of ~ 25 and 13 km (Yang et al.,

200   2020; https://www.weather.gov/media/notification/pns20-44gfs_v16.pdf;

201   https://www.emc.ncep.noaa.gov/emc/pages/numerical_forecast_systems/gfs.php;

202   https://ufscommunity.org/wp-

203   content/uploads/2020/10/UFS_Webnair_GFSv16_20201022_FanglinYang.pdf).

205   **Figure 1.** The a) native FV3 gnomonic cubed-sphere grid at C48 (2-degree) resolution (image
206   courtesy of Dusan Jovic, NOAA) and b) vertical resolution (P vs. dP) for the upgraded GFSv16
207   (green) compared to the previous GFSv15.3 (blue) and the European Centre for Medium-Range
208   Weather Forecasts (ECMWF) model (black).
209
210
211   The GFSv16 has significantly improved its physical parameterizations (e.g., Planetary

212   Boundary Layer (PBL), gravity wave, radiation, clouds and precipitation, land surface, and

213   surface layer schemes) and upgraded to the Global Data Assimilation System (GDAS) Version

214   16 (Yang et al., 2020; https://www.weather.gov/media/notification/pns20-44gfs_v16.pdf;

215   https://www.emc.ncep.noaa.gov/emc/pages/numerical_forecast_systems/gfs.php;

216   https://ufscommunity.org/wp-

217   content/uploads/2020/10/UFS_Webnair_GFSv16_20201022_FanglinYang.pdf).

218   The global GFSv16 has changed format of forecast output history files from binary

219   (nemsio) to netCDF with zlib compression (data volume reduced by about 60%), and provides

220   the *hourly* (important for CMAQ predictions) output for a 72-hour (3-day) forecast each day.

221   The prior operational NAQFC (NMMB-CMAQ) forecast is only out to 48 hours (2-day). The

222   netCDF output is available (via live disk and archives) to all of NOAA's downstream model

223   applications, and is in the form of a Gaussian, rectangular grid with a global-uniform grid

224   resolution of ~13 km (referred to as "C768"), with a set number of latitude and longitude

225   coordinates. The NOAA GFDL website provides more information about FV3 and its grids

226   (https://www.gfdl.noaa.gov/fv3/). There are additional new surface fields in the GFSv16 output,

227   which include plant canopy surface water, surface temperature and moisture at four below-

228   ground levels (0-0.1, 0.1-0.4, 0.4-1, 1-2 m), surface roughness, soil and vegetation type, and

229   friction velocity.

230   *2.1.2 The NOAA-EPA Atmosphere Chemistry Coupler (NACC)*
231
232   The meteorological-chemical coupling of the GFSv16 to the regional, state-of-the-science

233   CMAQ *v5.3.1* model (U.S. EPA, 2019; Appel et al., 2021) is achieved via the NOAA-EPA

234   Atmosphere Chemistry Coupler (NACC) version 1 (NACC, i.e., *"knack": meaning an acquired*

235   *skill*), which is adapted from the U.S. EPA's Meteorology-Chemistry Interface Processor (MCIP)

236   version 5 (Otte and Pleim, 2010; https://github.com/USEPA/CMAQ). The NACC and CMAQ

237   coupling (hereafter referred to as NACC-CMAQ) involves a number of structural and scientific

238   advancements (Figure 2; "The Advanced NAQFC") compared to the previous operational

239   NMMB-CMAQ; hereafter referred to as "prior NAQFC".
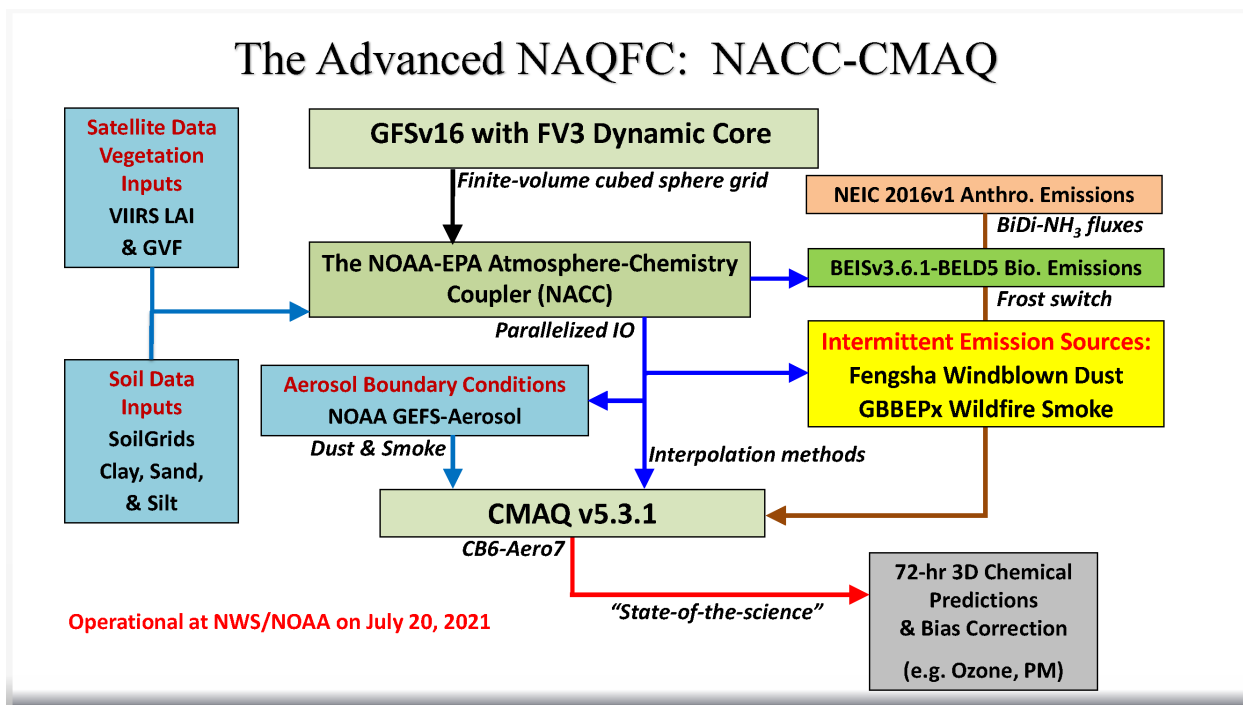
Figure 2. Schematic of the advanced NAQFC based on NACC-CMAQ.

The major structural changes to NACC-CMAQ include a variable-dependent bilinear or nearest-neighbor horizontal interpolation of the GFSv16 Gaussian gridded (~13 km) fields (e.g., 2-m temperature, 2-meter specific humidity, 10-m wind speed and direction, and sea level pressure) to Lambert Conic Conformal (LCC) at 12-km horizontal grid spacing (same as the prior NAQFC) (Figures 3a-b). NACC-CMAQ also includes a redefined vertical structure based on vertical interpolation (i.e., collapsing) to a 35-layer configuration (Figure 3c) that is identical to the prior NAQFC.
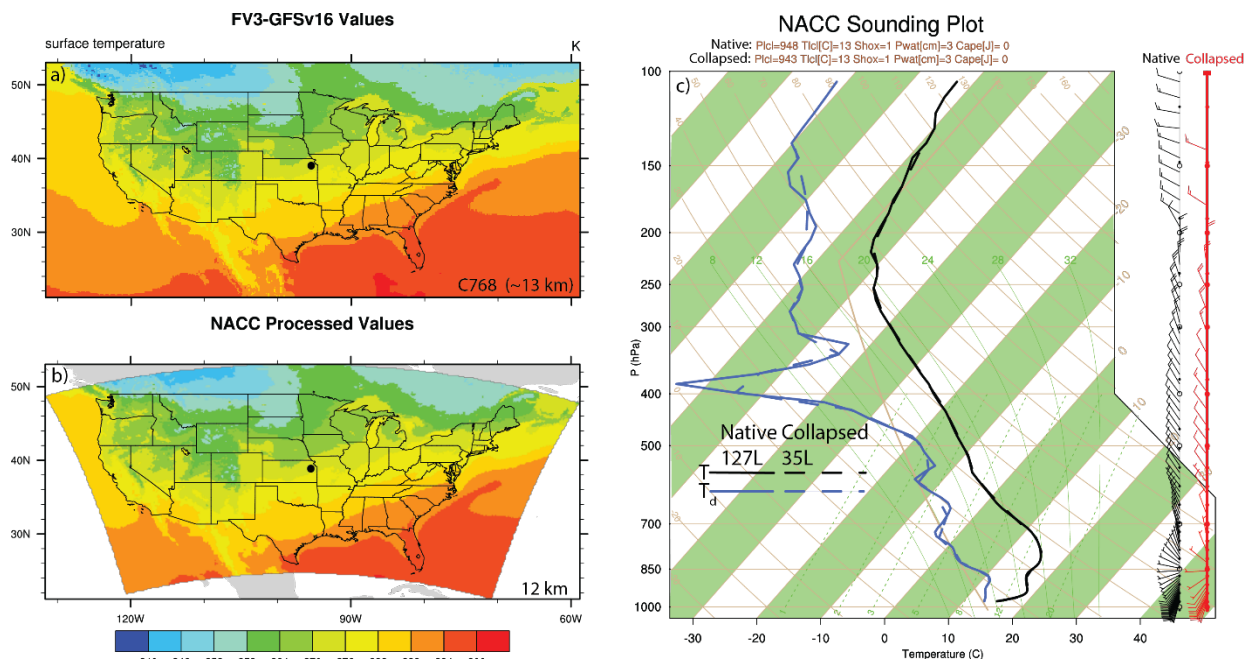
Figure 3. Examples of the NACC-CMAQ a) GFSv16 Gaussian grid surface temperature (C768~13 km) and b) associated bilinear horizontal interpolation NACC LCC output (12 km), and c) Skew-T Log-P diagram of both GFSv16 native (127 layers; solid) and NACC interpolated (35 layers; dashed) profiles of temperature (black) and dewpoint (blue), and wind speed/direction (wind barbs; native=black and collapsed=red). The example sounding pertains to a date of September 24, 2020 at the closest model grid square to 39.07°N and 95.62°W (black dot in a)-b)).

Time-splitting techniques based on Message Passing Interface (MPI) commands

parallelize the GFSv16-to-NACC input and output (IO), which vastly improves the

computational efficiency for the updated 72-hr forecast period. The NACC-CMAQ coupling is

more unified and streamlined compared to prior NAQFC (Stajner et al., 2011; Lee et al., 2017;

Huang et al., 2017) and experimental GFSv15-CMAQ (Huang et al., 2018; 2019) applications,

while eliminating multiple pre- and post-processing steps. The NACC-CMAQ processing steps

are therefore subject to less uncertainty/error that comes with multiple grid interpolations and

restructuring used previously, and are more computationally efficient for the 72-hr forecast

window. Furthermore, the vertical interpolation from 127 to 35 layers results in an excellent

agreement in the vertical structure of key atmospheric state variables (Figure 3c). While this

example is only for the central U.S., other model grid cell locations in the east and west U.S. also

270 demonstrate excellent agreement in the native and collapsed vertical structure in NACC (not

271 shown). The NACC-CMAQ domains for Alaska and Hawaii remain under development, so this

272 paper focuses only on the results inside the CONUS domain.

273   The left side of Figure 2 shows that NACC-CMAQ incorporates high resolution satellite

274 data for a 2018-2020 climatological (12-month) averaged leaf area index (LAI), which is based

275 on the Visible Infrared Imager Radiometer Suite (VIIRS) 8-day, Level 4 Global 500 m SIN Grid,

276 V001 product (Myneni and Knyazikhin, 2018; https://lpdaac.usgs.gov/products/vnp15a2hv001/).

277 This is a substantial update from the prior NAQFC, which assumed an unrealistic static value of

278 LAI = 4 across the entire domain. The NOAA product for near-real-time (NRT) greenness

279 vegetation fraction (GVF) from VIIRS (Ding and Zhu, 2018;

280 https://www.ospo.noaa.gov/Products/land/gvf/) is used as a dynamic, direct input in NACC-

281 CMAQ instead of using the GFSv16 vegetation fraction (VEG). Both VIIRS LAI and GVF are

282 preprocessed, and NACC performs nearest-neighbor interpolation to the NAQFC grid.

283   More realistic land cover characteristics have shown to improve modeled meteorology,

284 chemistry, and surface-atmosphere exchange processes in the coupled Weather Research and

285 Forecasting (WRF; Powers et al., 2017; Skamarock & Klemp, 2008)-CMAQ model (e.g., Ran et

286 al., 2016; Campbell et al., 2019). Test results here show that rapid-refresh of high resolution

287 VIIRS LAI and GVF in NACC have distinct differences compared to an older 2010 MODIS-

288 International Geosphere-Biosphere Programme (IGBP) LAI climatology and GFSv16-based

289 VEG, respectively (Figs. S1-S2). The updated, dynamic LAI and GVF alter biogenic emissions,

290 dry deposition, and resulting concentrations of gases and aerosols in NACC-CMAQ, particularly

291 during the fall transition month of October 2020 (Fig. S3).

292   NACC-CMAQ also uses global, gridded soil information based on the 2019 SoilGrids^{TM}

293   250-m resolution data (https://www.isric.org/explore/soilgrids) to drive an inline FENGSHA

294   Windblown dust model (Fu et al., 2014; Huang et al., 2015; Dong et al., 2016) in NACC-CMAQ

295   (Figure 2). Section 2.2 below provides more information on the specific parameters used in

296   FENGSHA.

297   As in the operational NAQFC, the chemical initial conditions are taken from the previous

298   day's (CMAQ) forecast output, and a NRT bias-correction using AirNow surface observations

299   (https://www.airnow.gov/) is applied to the 72-hr predictions of O_3 and $PM_{2.5}$ (Figure 2). Huang

300   et al. (2017) provides more information on the bias-correction technique.

301   2.2 Updated Chemistry, Emissions, and Air-Surface Exchange Processes
302
303   *2.2.1 The Community Multiscale Air Quality (CMAQ) Model, Version 5.3.1*
304
305   A major update in NACC-CMAQ is coupling the GFSv16 to a "state-of-the-science"

306   chemical transport model, CMAQv5.3.1 (U.S. EPA, 2019; Appel et al., 2021) (Figure 2). The

307   prior NAQFC and experimental GFSv15-CMAQ both use CMAQv5.0.2, released in April 2014

308   (U.S. EPA, 2014). The major release of CMAQv5.3 incorporates significant improvements to

309   gas chemistry (e.g., halogen-mediated ozone loss), aerosol modules (e.g., improved secondary

310   organic aerosol formation), photolysis rates, aqueous and heterogeneous chemistry, transport

311   processes, air-surface exchange, emissions, and other structural and computational improvements

312   (Appel et al., 2021). The use of CMAQv5.3.1 in NACC-CMAQ also contains a number of bug

313   fixes to v5.3. Version 6 of the Carbon Bond (CB6) mechanism is used for gas-phase chemistry

314   (Yarwood et al., 2010), and the updated U.S. EPA's AERO7 module is used for aerosol

315   formation in NACC-CMAQ. The U.S. EPA's GitHub webpage

316 (https://github.com/USEPA/CMAQ/blob/master/DOCS/Release_Notes/README.md) contains

317 the CMAQv5.3 and v5.3.1 release notes, mechanism descriptions, and enhancements.

318 *2.2.2 National Emissions Inventory Collaborative (NEIC) 2016v1 Emissions*
319
320 The anthropogenic emissions modeling data may be the most influential input for chemical

321 transport model predictions in any AQF system (Matthias et al., 2018). The model emissions are

322 updated from National Emissions Inventory (NEI) 2014 version 2 that is used by the prior

323 NAQFC to NEI Collaborative (NEIC) 2016v1 Emissions Modeling Platform (NEIC, 2019),

324 which is based on updated models and datasets applied to the U.S. Environmental Protection

325 Agency's (EPA) NEI2014v2. The prior NAQFC uses an older NEI2014v2 emissions dataset.

326 There have been substantial updates to the NEIC2016v1, which include emission decreases for

327 CO, NO_x, SO_2, and $PM_{2.5}$, and increases in total VOC and ammonia (NH_3) emissions compared

328 to the NEI2014v2 (NEIC, 2019). The intermittent, "event-based" emissions from wildfires and

329 windblown dust, as well as persistent biogenic emissions sources are not from the NEIC2016v1,

330 but rather are dynamically predicted inline within NACC-CMAQ (described in following

331 sections). The NEIC2016v1 area-source (i.e., 2-D) emissions are gridded, netCDF/IOAPI format

332 that are interpolated to the 12-km NAQFC domain. The NEIC2016v1 also provides major point

333 source (i.e., 3D) emissions from six sectors: Commercial Marine Vehicles (CMV12 and

334 CMV3), Electricity Generating Units (EGUs), Non-EGUs, Oil-Gas sources, and "Other" point

335 sources. The anthropogenic point source plume rise is calculated inline within NACC-CMAQ

336 using the Briggs plume rise method (Briggs, 1965).   Slight adjustments are made to reduce the

337 anthropogenic aerosol/fugitive dust emissions over snow and wet soil surfaces to account for

338 different forecasted meteorology in GFSv16 compared to the conditions used in generating the

339 NEIC2016v1.

340   We note that the NEIC2016v1 emissions are not projected into the actual forecast year, with

341   the time lag being a long-recognized issue in NAQFC (e.g., Tong et al., 2012). Thus, the

342   NACC-CMAQ air quality simulations for the fall of 2020 and the winter of 2021 are impacted

343   by the COVID-19 pandemic, which resulted in significant changes to emission patterns and

344   ozone formation over the U.S. in 2020 and beyond (Campbell et al., 2021). In addition, mobile

345   source emissions have continued to decline since 2016 so it is likely that the emissions used in

346   the analysis do not entirely reflect recent changes to the emissions compared to 2016 (almost 5

347   years earlier). We are actively working to improve the representativeness of anthropogenic

348   emissions sources in NACC-CMAQ and next-generation versions of the NAQFC.

349   *2.2.3 Inline Biogenic Emissions and Bidirectional NH₃ Fluxes*

350   NACC-CMAQ uses the latest version of the Biogenic Emission Inventory System (BEIS)

351   v3.6.1 (Vukovich and Pierce, 2002; Schwede, 2005) for estimating the biogenic VOC (BVOC)

352   emissions. BEISv3.6.1 includes updated vegetation inputs and advanced two-layer canopy

353   model formulations for estimating leaf (sun and shade) temperatures and vegetation data (Weiss

354   and Norman, 1985; Campbell and Norman, 1998; Niinemets et al., 2010; Bash et al., 2015).

355   NACC-CMAQ also uses the revised Biogenic Emissions Landuse Dataset v5 (BELD5), which

356   includes a newer version of the Forest Inventory and Analysis (FIA) version 8.0 and updated

357   agricultural land use from the 2017 U.S. Department of Agriculture (USDA) crop data layer.

358   The BELD5 dataset also uses a MODIS 21-category land use dataset with lakes identified

359   separately from oceans. The prior NAQFC used a much older BELD3 version.

360   The prior NAQFC also only considered summer factors in BEIS, and did not capture

361   seasonal (summer and winter) changes to the normalized biogenic emissions factors (vegetation

362   species-specific). NACC-CMAQ is improved and uses a new "vegetation frost switch" that

363 adjusts between summer and winter normalized emission factors in BEISv3.6.1 based on the

364 calendar date and 2-m temperature (TEMP2). In NACC, a new time-dependent variable,

365 'SEASON' is equal to one during the growing season, or equal to zero outside the growing

366 season. The SEASON is (boreal) summer if the calendar date is on or between 15 April and 15

367 October, but switches to winter if TEMP2 drops below 28°F, and is winter if the date is on or

368 between 16 October and 14 April, but switches to summer if TEMP2 rises above 32°F.   Thus,

369 the SEASON variable in NACC-CMAQ differs from typical retrospective CMAQ applications,

370 and is more dynamic with hourly variability based on the GFSv16 forecasted TEMP2. Test

371 results show generally improved model performance for all U.S. regions in December 2020

372 (winter) with vegetation frost switch compared to using only summer season normalized

373 emissions (Table S1). Using BELD5 further improves model performance and reduces the error

374 in all CONUS regions compared to the older BELD3 used in December 2020 tests (Table S1).

375   NACC-CMAQ includes bidirectional NH_3 (BIDI-NH_3) for NH_3 fluxes (i.e., both

376 deposition and evasion) in the CMAQv5.3.1 "M3Dry" deposition model (Nemitz et al., 2000;

377 Cooter et al., 2010; Massad et al., 2010; Pleim and Ran, 2011; Bash et al., 2010, 2013; Pleim et

378 al., 2013; 2019). Here, the NH_3 fertilizer emissions are removed from the base NEIC2016v1

379 inventory to avoid double counting, as the inline BIDI-NH_3 module calculates these fluxes. The

380 BIDI-NH_3 module typically requires daily inputs (e.g., soil ammonia content, soil pH, soil

381 moisture, and other soil characteristics) from the USDA's Environmental Policy Integrated

382 Climate (EPIC) agroecosystem model (https://epicapex.tamu.edu/epic/; Williams et al., 1995) to

383 calculate the soil ammonia concentrations that are combined with air concentrations in CMAQ to

384 calculate BIDI-NH_3 fluxes. Typically, the Fertilizer Emission Scenario Tool (FEST-C,

385 https://www.cmascenter.org/fest-c/) processes the necessary meteorological conditions for

386 integration with the EPIC simulation for input to CMAQ (Ran et al., 2011; Cooter et al., 2012).

387 Use of the EPIC/FEST-C system is not feasible in an NRT operational forecasting model, and

388 thus we use a pre-generated, full-year 2011 EPIC/FEST-C simulation based on Campbell et al.

389 (2019) for the daily inputs to BIDI-NH$_3$ in NACC-CMAQ. NACC-CMAQ directly uses the

390 GFSv16 soil moisture conditions in place of the FEST-C processed soil conditions required for

391 the latest version of BIDI-NH$_3$ in CMAQv5.3.1 (Pleim et al., 2019).

392   *2.2.4 Inline Wildfire Smoke and Windblown Dust Emissions*
393
394   Wildfires have been increasing in size (Westerling et al., 2006) and potentially in severity

395 (Miller et al., 2009) over the past decades. Wildfire smoke outbreaks can lead to extreme

396 concentrations of PM$_{2.5}$ and enhanced O$_3$, and are major concerns for air quality forecasting and

397 consequential human and ecosystem health impacts. NACC-CMAQ includes a new inline

398 calculation of wildfire smoke emissions based on the Blended Global Biomass Burning

399 Emissions Product (GBBEPx V3; Zhang et al., 2012, 2014). GBBEPx provides hourly global

400 biomass burning emissions (PM$_{2.5}$, BC, OC, NO$_x$, NH$_3$, CO, and SO$_2$). It blends fire

401 observations from two sensors, including the Moderate Resolution Imaging Spectroradiometer

402 (MODIS) on the NASA Terra and Aqua satellites, and the Visible Infrared Imaging

403 Spectrometer (VIIRS) on the Suomi National Polar-orbiting Partnership (SNPP) and Joint Polar-

404 orbiting Satellite System 1 (JPSS1) satellites. The GBBEPx data are further processed to prepare

405 model-ready emission datasets. First, the 0.1 x 0.1 degree latitude/longitude data are converted

406 into the NAQFC LCC projection. U.S. EPA-based Sparse Matrix Operator Kernel Emissions

407 (SMOKE) fire speciation and diurnal profiles provide the PM speciation and diurnal patterns in

408 NACC-CMAQ, respectively, while both landuse and region are used to identify fire types. The

409 fire duration persists for the 72-hour forecast period (with scaling of 1.0, 0.25, and 0.25 for day

410 1, 2, and 3, respectively) for wildfires identified when the grid cell forest fraction is > 0.4. In the

411 eastern U.S. (longitude east of 100°W), however, the fires are assumed to be mainly prescribed

412 burns in forested regions that only persist for the first 24-hours. The wildfire plume rise is

413 calculated inline within NACC-CMAQ using either the Briggs (1965) or Sofiev et al. (2012)

414 algorithms (Wilkins et al. 2019); currently the Briggs method is used by default.

415   Climate models project warming and drying trends in the southwestern U.S., where

416 intermittent windblown dust storms are becoming more frequent with the occurrence of drought

417 (Tong et al., 2017), or even "megadrought" conditions (Williams et al., 2020). Windblown dust

418 storms can lead to extreme levels of coarse mode particulate matter (i.e., PM_{10}), and cause

419 detrimental effects to human and agroecosystem health and visibility. NACC-CMAQ includes a

420 novel inline methodology for calculating windblown dust, based on the FENGSHA model

421 (Huang et al., 2015; Dong et al., 2016). In NACC-CMAQ, the potential for vertical dust flux in

422 FENGSHA is generally controlled by the sediment supply map (SSM), and the magnitude of the

423 friction velocity (USTAR) compared to a threshold friction velocity (UTHR) that determines the

424 USTAR needed to transfer dust from soil surfaces to the atmosphere. The UTHR is dependent on

425 the land cover and soil type, as well as the soil moisture. The SoilGrids^{TM} 250-m high-resolution

426 dataset (https://www.isric.org/explore/soilgrids) provides the necessary clay, silt, and sand

427 fractions used to calculate the SSM. Tang et al. (2022) further evaluates GBBEPx wildfire

428 smoke during air quality events predicted by NACC-CMAQ.

429 2.3 Updated Dynamic Aerosol Boundary Conditions
430
431   The chemical lateral boundary conditions (CLBCs) are critical to the prediction accuracy of

432 regional chemical transport models, particularly during intrusion events (Tang et al., 2009;

433 2021a). The CLBCs represent the spatiotemporal distribution of chemical species along the

434 lateral boundaries of the domain of a regional model. NACC-CMAQ uses methods described in

435 Tang et al. (2021) and implements dynamic CLBCs (updated every 6-hours) for dust and smoke

436 aerosol data that are extracted (and mapped to CMAQ CB6-Aero7 species) from the NOAA

437 operational global atmospheric aerosol model, known as the Global Ensemble Forecast-Aerosols

438 (GEFS-Aerosols) member (Figure 2). GEFS-Aerosols is also based on the FV3GFS dynamical

439 core, which uses the Goddard Chemistry Aerosol Radiation and Transport (GOCART) model for

440 its sulfate, dust, BC, OC, and sea-salt aerosol predictions (Chin et al.; 2000; 2002; Ginoux et al.,

441 2001). GEFS-Aerosols uses the same wildfire smoke and windblown dust dataset/algorithms as

442 in NACC-CMAQ.   The operational version of GEFS-Aerosols is run by the NWS as a special

443 unperturbed forecast of the Global Ensemble Forecast System version 12

444 (https://www.ncdc.noaa.gov/data-access/model-data/model-datasets/global-ensemble-forecast-

445 system-gefs), which provides an ensemble forecast product four times per day. Dynamic CLBCs

446 capture the signals of aerosol intrusion events such as biomass burning or windblown dust

447 plumes from outside the domain, which can improve the prediction accuracy of downstream O_3

448 and $PM_{2.5}$ concentrations at the surface (Tang et al., 2021a).

449 **3. Simulation Design and Evaluation Protocol**

450
451   Table 1 summarizes the GFSv16/NACC-CMAQv5.3.1 model configuration described in

452 Section 2, as well as some additional model details. The model components and configurations

453 used in prior NAQFC system are summarized in Table S2 (based on Lee et al., 2017) for

454 comparison.

455

456

457   **Table 1. GFSv16/NACC-CMAQv5.3.1 model components and configurations.**

Model Attribute	Configuration	Reference
Domain	Contiguous U.S.; Center = 40°N;97°W	n/a
Horizontal Resolution	12 km	n/a
Vertical Resolution	35 Layers from near-surface to about 14 km (~ 60 hPa)	n/a
Meteorological ICs and BCs	FV3GFSv 16	https://nws.weather.gov/
Chemical ICs and BCs	2006 GEOS-Chem Simulation & GEFS-Aerosol Dynamic Smoke and Dust Aerosol CLBCs	http://acmg.seas.harvard.edu/geos/ *Tang et al.* (2021)
Anthropogenic Emissions	NEIC 2016v1 Platform	*NEIC* (2019)
Biogenic Emissions	Inline BEISv3.6.1 & BELD5	*Vukovich and Pierce* (2002)*; Schwede et al.* (2005)
Wildfire Emissions/Plume Rise	GBBEPxv3/ Inline Briggs	*https://www.ospo.noaa.gov/Products/land/gbbepx Briggs* (1965)
Microphysics	GFDL six-category cloud microphysics scheme	*Lin et al., 1983; Lord et al., 1984; Krueger et al., 1995; Chen and Lin, 2011; Chen and Lin, 2013*
PBL Physics Scheme	sa-TKE-EDMF	*Han and Bretherton (2019)*
Shallow/Deep Cumulus Parameterization	SAS Scheme	*Han et al. (2011; 2017)*
Shortwave and Longwave Radiation	RRTMg	*Mlawer et al. (1997); Clough et al. (2005); Iacono et al. (2008)*
Land Surface Model	Noah Land Surface Model	*Chen and Dudhia (2001), Ek et al. (2003), Tewari et al. (2004)*
Surface Layer	Monin-Obukhov	*Monin-Obukhov* (1954)*; Grell et al.* (1994)*; Jimenez et al.* (2012)
Gas-phase Chemistry	CB6	*Yarwood et al., 2010*
Aqueous-phase Chemistry	CMAQ AQCHem Updates	*Martin and Good* (1991)*; Alexander et al.* (2009)*; Sarwar et al.* (2011)
Aerosol Module/Size	AERO7	*Appel et al.* (2021)
Other Model Attributes	-In-line Photolysis	*Binkowski et al.* (2007)

	-In-line Bi-Directional NH$_3$ Exchange	*Nemitz et al., 2000; Cooter et al., 2010; Massad et al., 2010; Pleim and Ran, 2011; Bash et al., 2010, 2013; Pleim et al., 2013; 2019*
	-In-line FENGSHA Wind-Blown Dust Emissions	*Fu et al., 2014; Huang et al., 2015; Dong et al., 2016*
	-In-line Sea-salt Emissions	*Kelley et al.* (2010)

458

459   The simulation design consists of evaluations of one-month, continuous NACC-CMAQ

460 (72-hr, 3-day forecast) and prior NAQFC (48-hr, 2-day forecast) simulations for September 2020

461 (late summer/fall period) and January 2021 (winter period) (with previous 1-month spin-up and

462 training-data period) over CONUS at a horizontal grid spacing of 12 km (Table 1). September

463 2020 is used for the warm season because it is the closest month to summer when both the

464 NACC-CMAQ and prior operational NAQFC systems were simultaneously run. The prior

465 operational NAQFC was discontinued on July 20, 2021 due to computational constraints at

466 NWS/NOAA.

467   The Surface Weather Observations and Reports for Aviation Routine Weather Reports

468 (METAR), collected by NCEP's Meteorological Assimilation Data Ingest System (MADIS)

469 (https://madis.ncep.noaa.gov/madis_metar.shtml), provide observations of TEMP2, 2-m specific

470 humidity (Q2), and 10-m wind speed (WSPD10). The World Radiation Monitoring Center's

471 (WRMC's) Baseline Solar Radiation Network (BSRN) (https://

472 bsrn.awi.de/; Driemel et al., 2018) and U.S. Surface Radiation Network (SURFRAD;

473 https://gml.noaa.gov/grad/surfrad/) provide shortwave radiation observations at the ground

474 (SWDOWN). The PRISM Climate Group, Northwest Alliance for Computational Science and

475 Engineering, at Oregon State University (https://prism.oregonstate.edu/l; Accessed on 05 May

476 2021) provide gridded total precipitation observations (PRECIP). The National Oceanic and

477   Atmospheric Administration (NOAA), Earth System Research Laboratory's (ESRL's)

478   Radiosonde Database (RAOB) (https://ruc.noaa.gov/raobs/) provide vertical profile observations

479   of temperature, relative humidity, and wind speed. The U.S. EPA Air Quality System (AQS;

480   https://www.epa.gov/aqs) and near-real-time AirNow observational networks

481   (https://www.airnow.gov/) provide near-surface O_3 and $PM_{2.5}$ measurements.

482   The statistical measures used to evaluate the meteorological-chemical/air quality

483   predictions include the mean bias (MB), normalized mean bias (NMB), normalized mean error

484   (NME), Root Mean Square Error (RSME), Anomaly Correlation Coefficient (ACC), Pearson's

485   correlation coefficient (R), and Index of Agreement (IOA). Statistical measures such as R, NMB,

486   and NME provide measures of the associativity (i.e., correlation), bias, and accuracy,

487   respectively, of specific modeled surface and vertical meteorology and surface O_3 and $PM_{2.5}$.

488   The meteorological and chemical evaluations use the publicly available U.S. EPA Atmospheric

489   Model Evaluation Tool (AMET; Appel et al., 2011) and NOAA/ARL Model and Observation

490   Evaluation Toolkit (MONET; Baker et al., 2017). A more detailed diagnostic evaluation for the

491   numerous science advancements (Figure 2) in NACC-CMAQ compared to the prior NAQFC, as

492   well as additional meteorological, trace gas, and $PM_{2.5}$ composition comparisons is shown in

493   Tang et al. (2022).

494   **4. Results**

495

496   4.1 Meteorological Analysis

497

498   Compared to NMMB used in the prior NAQFC, the GFSv16 model has lower actual

499   TEMP2 in the east-southeast and parts of the northwest (Figures 4a-d), but has higher TEMP2 in

500   the central, northern plains, and parts of the west-southwest U.S. with higher 10-meter wind

501   speeds (WSPD10) in these regions (Figures 4i-l). GFSv16 is drier with widespread lower 2-

502   meter specific humidity (Q2; Figures 4e-h) and lower cloud fractions (CFRAC) (Figures 4m-p),

503   higher solar radiation absorbed at the ground (GSW; Figures 5a-d), lower longwave radiation

504   absorbed at the ground (GLW; Figures 5e-h), deeper planetary boundary layer height (PBLH;

505   Figures 5i-l), and generally more regions of increased precipitation (PRECIP; Figures 5m-p).

506   Differences in the CFRAC are (in part) impacted by differences in the model definition of cloud

507   cover; NMMB uses a binary cloud cover definition at each grid point, while GFSv16 uses

508   fractional cloud cover to calculate CFRAC. The PBLH in the prior NAQFC is re-diagnosed

509   based on the Troen and Mahrt (1986) incremental calculation of the bulk Richardson number

510   (Ri_b) from the surface up to a height above the neutral buoyancy level in the Asymmetric

511   Convective Model v2 (ACM2) PBL scheme in CMAQ (Pleim 2007a;2007b). NACC-CMAQ

512   directly uses the diagnosed PBLH from the Turbulent Kinetic Energy (TKE)-based PBL scheme

513   in GFSv16 (Table 1; Han and Bretherton, 2019), which is also based on the Troen and Mahrt

514   (1986) Ri_b methodology with slight differences in some internal parameters (e.g., critical

515   Richardson number) compared to ACM2.
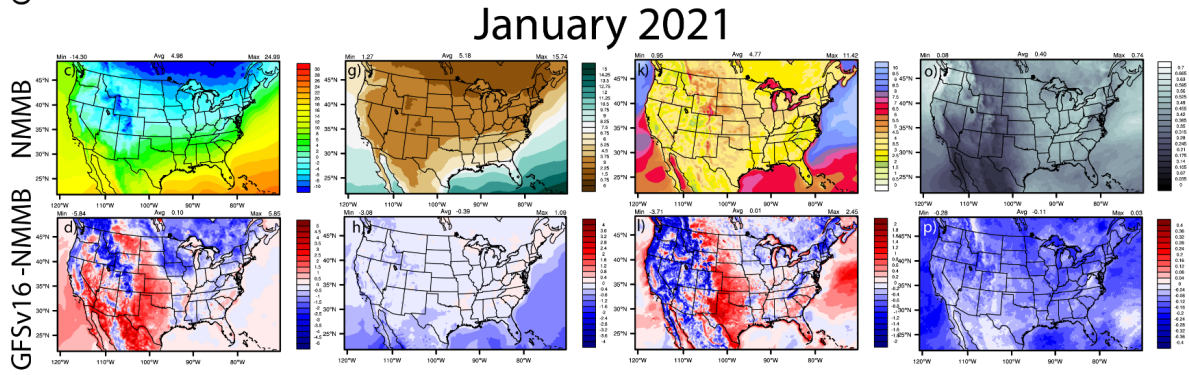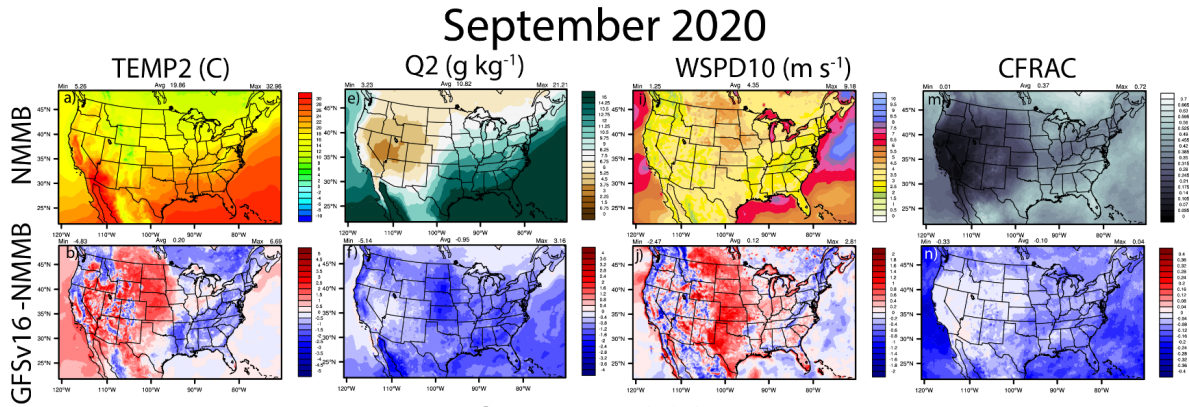
Figure 4. September 2020 and January 2021 spatial average plots for NMMB (prior NAQFC) and the absolute differences for GFSv16 (NACC) - NMMB for TEMP2, Q2, WSPD10 and CFRAC.
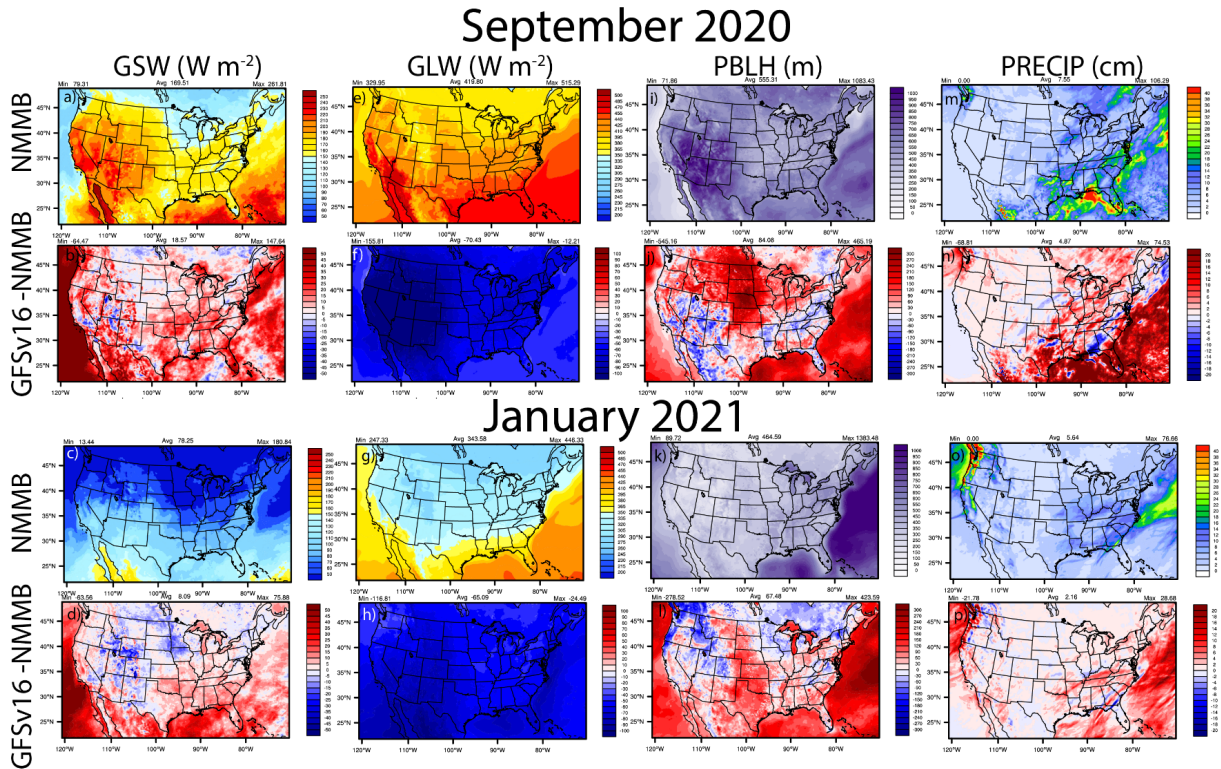
Figure 5. Same as in Figure 4 but for GSW, GLW, PBLH, and PRECIP.

523   The GFSv16 (NACC) and re-diagnosed ACM2 (prior NAQFC) diurnal PBLH patterns are

524   similar at night; however, the GFSv16 PBLH is considerably higher than the prior NAQFC

525   during the daytime for all regions in September and January (Supporting Figures S4-S5).

526   The meteorological differences between GFSv16 and NMMB (Figures 4-5) influence

527   chemical predictions in CMAQ, which include a deeper daytime PBL and more precipitation that

528   can effectively dilute the gaseous and aerosol concentrations for NACC-CMAQ in some regions

529   across CONUS.   Areas of lower CFRAC and higher TEMP2 and GSW in GFSv16, however,

530   will increase photolysis and daytime O_3 formation in NACC-CMAQ in certain regions including

531   the south and upper Great Plains U.S. Considering the PBLH calculation methodologies are

532   similar between the prior NAQFC and NACC-CMAQ (based on Troen and Mahrt (1986) with

533   differences in some internal parameters), the differences in near-surface meteorology (i.e.,

534   generally warmer/drier) conditions in the GFSv16 (Table 2 and Table S2) are driving the

535   differences in PBLH (Figures 5i-l). These differences affect the pollutant mixing and dilution,

536   and in part, the resulting air quality predictions between the prior NAQFC and NACC-CMAQ

537   (see Section 4.4 below).

538

539   4.2 Meteorological Evaluation and Metrics
540

541   Evaluation of the simulated day 1 (0-24 hr) forecasted meteorology against the METAR

542   network shows that GFSv16 generally has a higher positive TEMP2 (warmer) bias (Figure 6) in

543   the west, and has a CONUS-wide higher negative Q2 (dry) bias (Figure 7) compared to prior

544   NMMB (i.e., prior NAQFC) in both September and January.
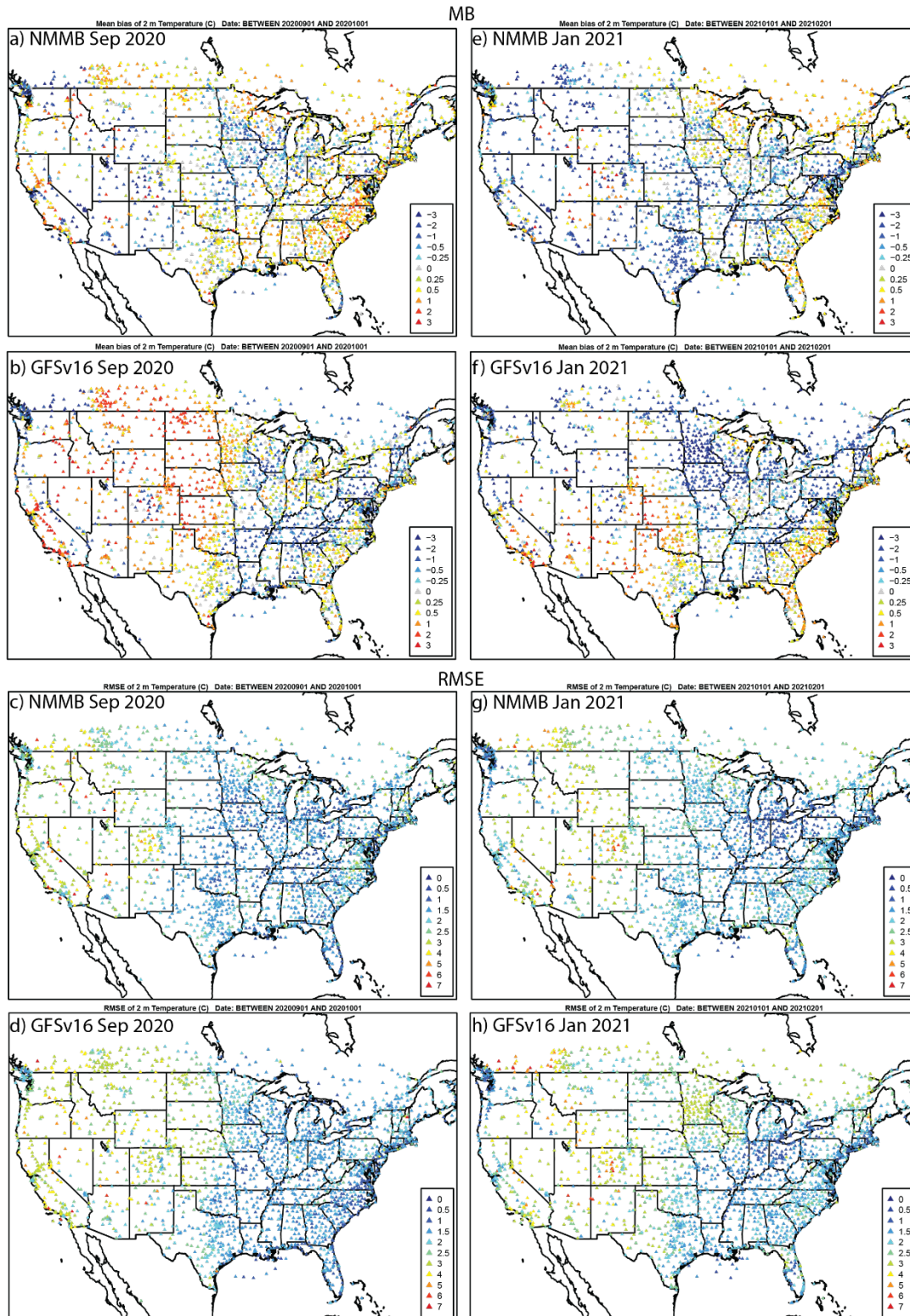
Figure 6. Average day 1 (0-24 hr) forecasted TEMP2 MB (°C) and RMSE (°C) for NMMB and GFSv16 during a)-d) September 2020 and e)-h) January 2021 compared to METAR observations.
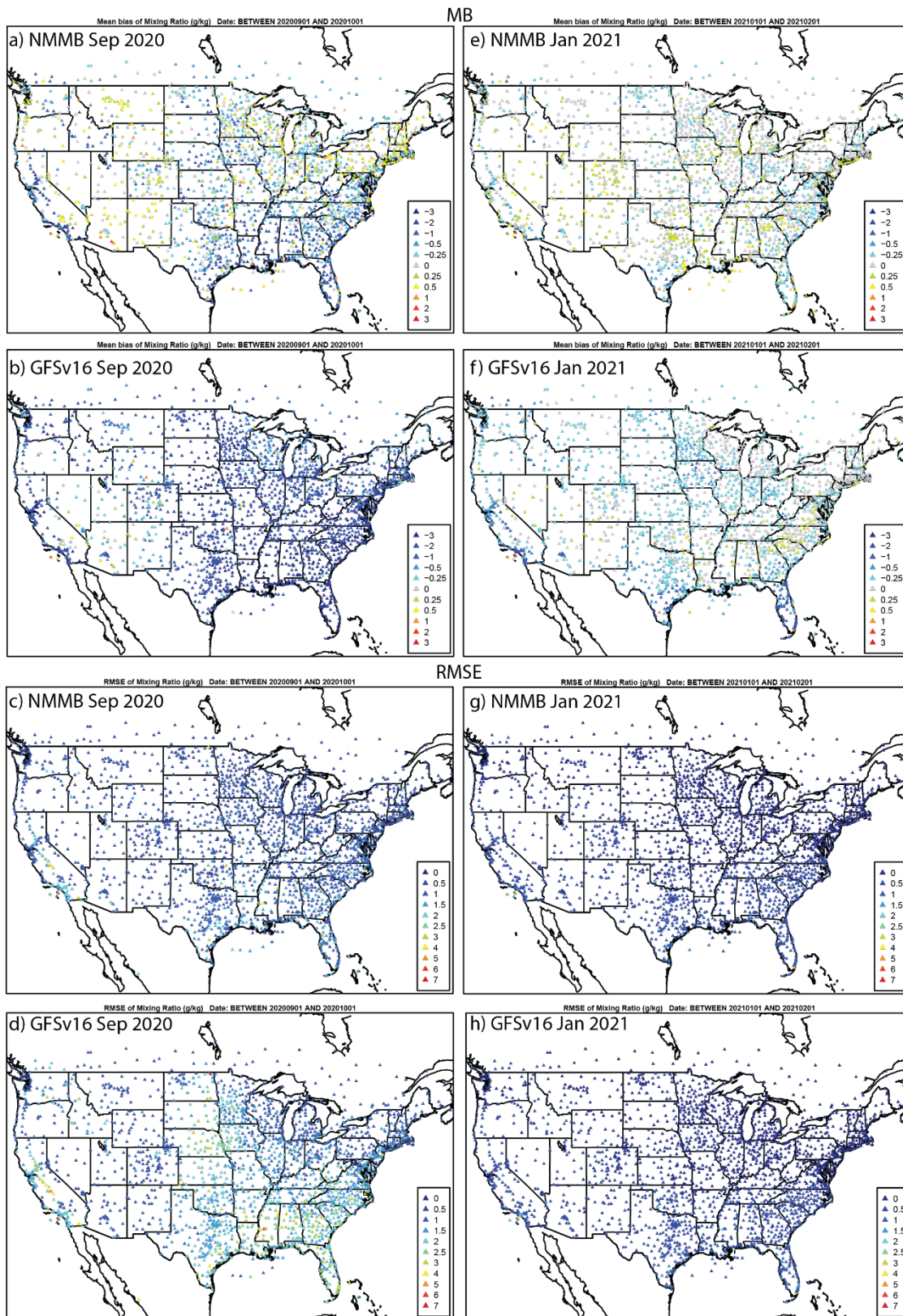
Figure 7. Same as in Figure 6, but for Q2 (g kg⁻¹).

551   There are regions of higher RMSE for T2 and Q2, and lower/degraded ACC (Figures S7-S8) for

552   GFSv16 compared to NMMB, especially in the southern and western CONUS regions during

553   September.   The spatial patterns and magnitudes of WSPD10 bias and error are similar between

554   GFSv16 and NMMB (Figure 8); however, the higher WSPD10 for GFSv16 in the southern and

555   central CONUS leads to a shift from negative to positive biases from Texas northward to North

556   Dakota, especially during September. The WSPD10 RMSE is higher (Figure 8) and the ACC is

557   also lower/degraded (Figure S9) for GFSv16 in those regions, otherwise, the GFSv16 and

558   NMMB have similar performance for WSPD10. The day 1 forecast model performance (MB,

559   RMSE, and ACC) for 10-m wind direction (WDIR10) is similar between NMMB and GFSv16 in

560   both September and January (Figs. S6 and S10).
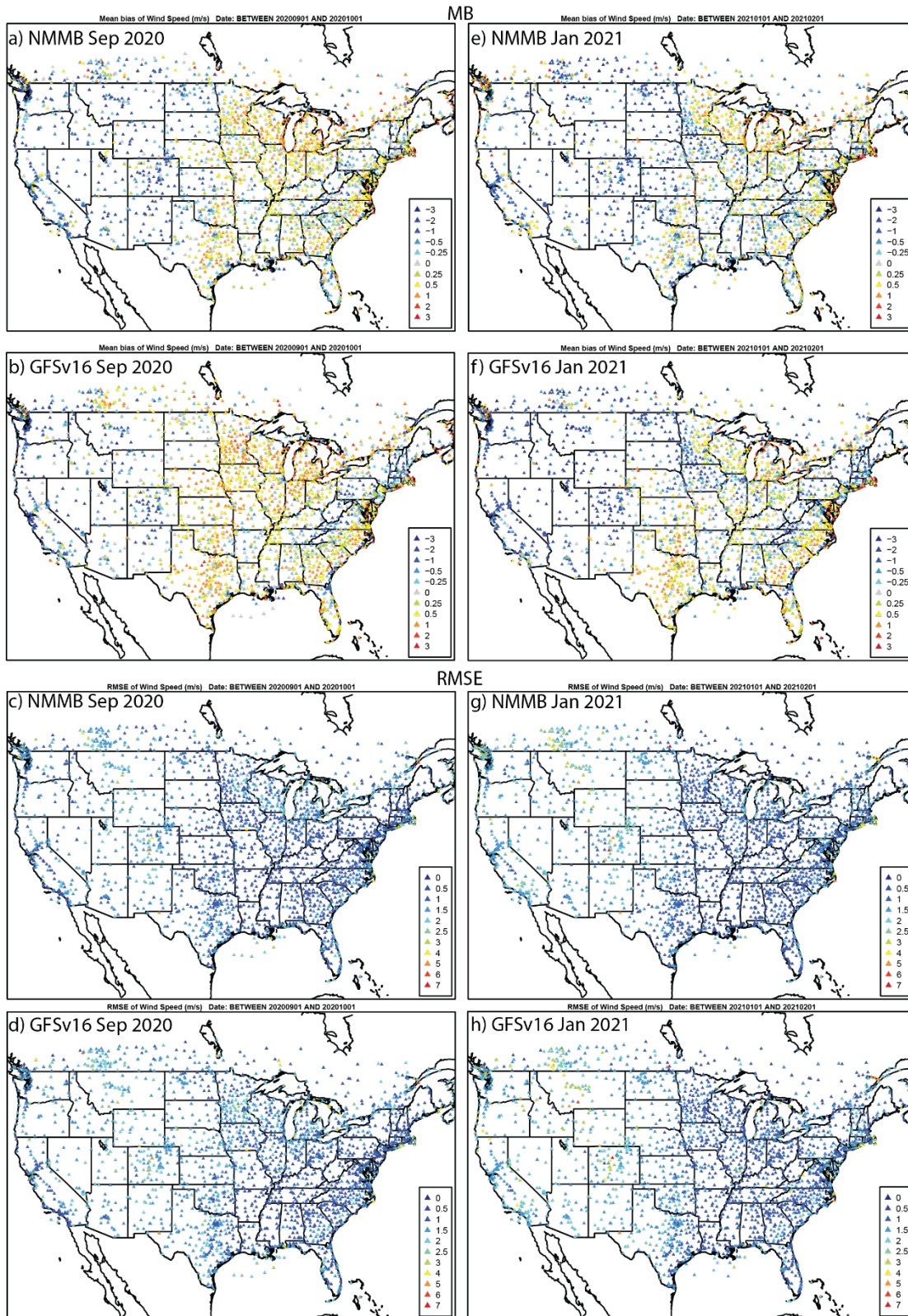
Figure 8. Same as in Figure 6, but for WSPD10 (m s^{-1}).

563   Overall, the GFSv16 results are favorable for driving the advanced NACC-CMAQ

564   system, with some areas of concern in the degraded TEMP2 and Q2 in the warmer/drier regions,

565   particularly in the south and west CONUS during September. This roughly correlates with

566   warmer/drier top-layer soil conditions in GFSv16 in these regions (Fig. S11), and thus land

567   surface/soil data assimilation and model development and improvement in GFSv16 is an active

568   area of focus at NOAA. The widespread dry bias in GFSv16 appears to be persistent, as an

569   independent evaluation of August 2019 demonstrated very similar spatial patterns and magnitude

570   of Q2 underpredictions in the eastern half of CONUS compared to the METAR network (not

571   shown).

572   The GFSv16-driven NACC-CMAQ system extends out to a 72-hour forecast. Hence,

573   there is a question of how the day 1 and 2 forecasts perform for NMMB vs. GFSv16 in the

574   eastern (<100° W) and western (>100° W) U.S., and how a day 3 forecast extension also affects

575   the GFSv16 diurnal and statistical model performance. The GFSv16/NACC diurnal patterns of

576   standard deviation, error, and bias for TEMP2, Q2, and WSPD10 are very similar to each other

577   for days 1-3 (Figures S12-14). While there is a slight increase in error and decreased correlation

578   (R), the relevant statistical metrics (e.g., MB, NMB, RMSE, and R) do not change appreciably

579   from day 1 to 3 for both September and January (Tables S3-S4). This lends confidence in the

580   utility of using the updated GFSv16 meteorology to drive a 72-hour air quality forecast in

581   NACC-CMAQ.

582   The day 1 diurnal statistics highlight both similar and contrasting TEMP2 and Q2

583   patterns for NMMB vs. GFSv16 in the eastern and western CONUS (Figures S12-S13). In

584   September (Figure S12a), NMMB has higher error and positive TEMP2 (i.e., warm) bias in

585   eastern CONUS during morning hours, and lower error with a slight cool bias in the

586   afternoon/evening, while GFSv16 shows slight overpredicted TEMP2 during most hours of the

587   day in the east. Over western CONUS, there are larger diurnal TEMP2 differences that include

588   small oscillating TEMP2 biases (about zero) for NMMB, along with distinctly large warm biases

589   during all daytime hours for GFSv16 in the west. There are larger error and negative Q2 (i.e.,

590   drier) biases for GFVSv16 compared to NMMB in eastern and western CONUS (Figure S13a).

591   In January, the TEMP2 and Q2 diurnal statistical patterns are similar for NMMB and GFSv16 in

592   both the eastern and western CONUS; however, the GFSv16 daytime hours have slightly higher

593   error and warmer and drier biases compared to NMMB (Figures S12b and S13b).

594   The total PRECIP is generally higher in GFSv16 compared to NMMB out East (Figure

595   5), which leads to larger overpredictions on average in CONUS compared to PRISM (Figure 9).

596   GFSv16 has a positive PRECIP bias on average in CONUS, NMMB has a negative bias, and

597   there is relatively more difference in the spatial patterns between NMMB and GFSv16 for

598   September compared to January. The difference is impacted by higher convective activity

599   during late summer/early fall in September compared to winter in January (not shown). Further

600   analysis indicated that generally heavier PRECIP reduces the predicted $PM_{2.5}$ concentrations via

601   wet deposition (not shown) in the east-southeast, and in parts of the west-northwest compared to

602   NMMB.

603
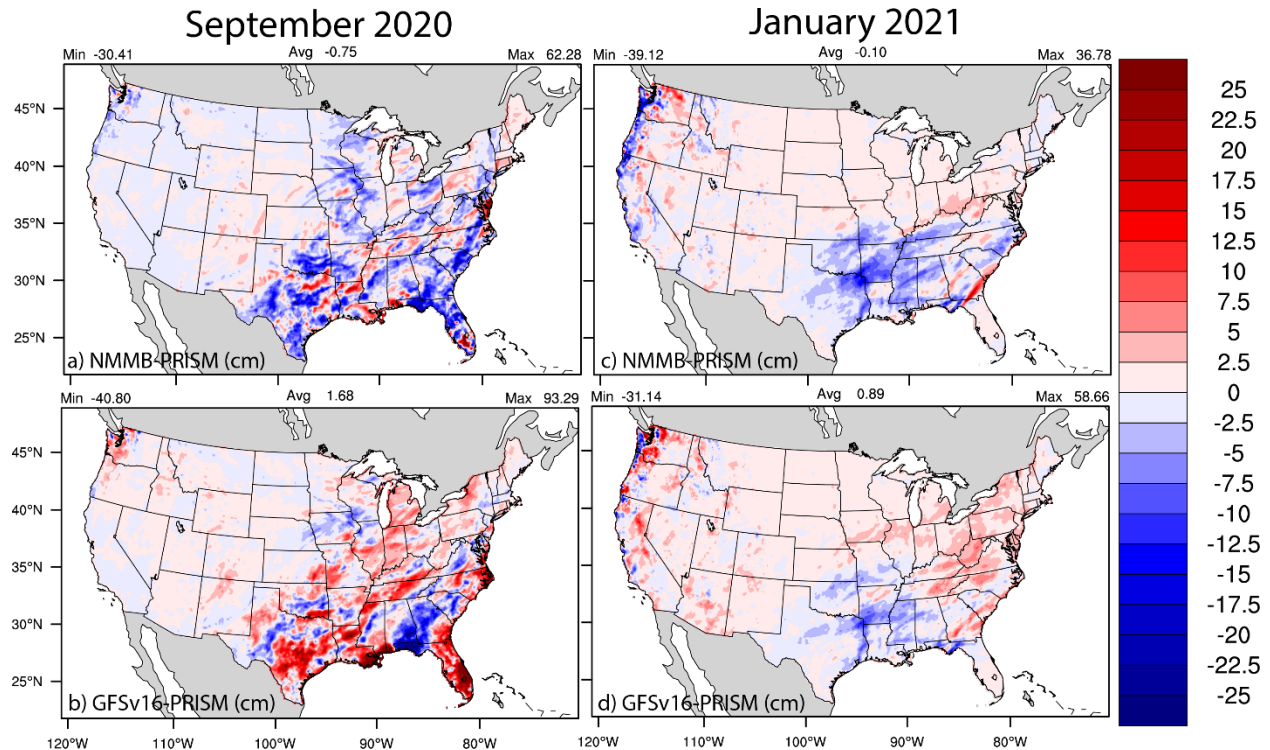
Figure 9. Average day 1 (0-24 hr) forecasted total PRECIP (cm) biases (Predicted-PRISM) for NMMB (top) and GFSv16 (bottom) during a)-b) September 2020 and c)-d) January 2021.

Comparisons of the model vertical profile statistics (i.e., MB, RMSE, and IOA) for TEMP, RH, and WSPD against an average of select RAOB observations across CONUS indicate that the GFSv16 (NACC) performs consistently with the operational NMMB (NAQFC) column (Figure 10; IOA nearly identical at ~ 0.8-0.9). GFSv16 is warmer and drier than NMMB in the model layers near the surface (> 850 mb), especially in September; however, GFSv16 has a moister atmospheric column with higher wind speeds compared to NMMB above the surface and in the free troposphere (< 850 mb). Figures S15-S17 show the spatial variability across the different RAOB sites used in the average for Figure 10.   Analysis of the column (1000-250 hPa) average for all CONUS RAOB sites across CONUS indicate that GFSv16 has a predominantly cooler and moisture atmospheric column in September, despite being strongly warmer and drier near the surface (Figures S18-S19).
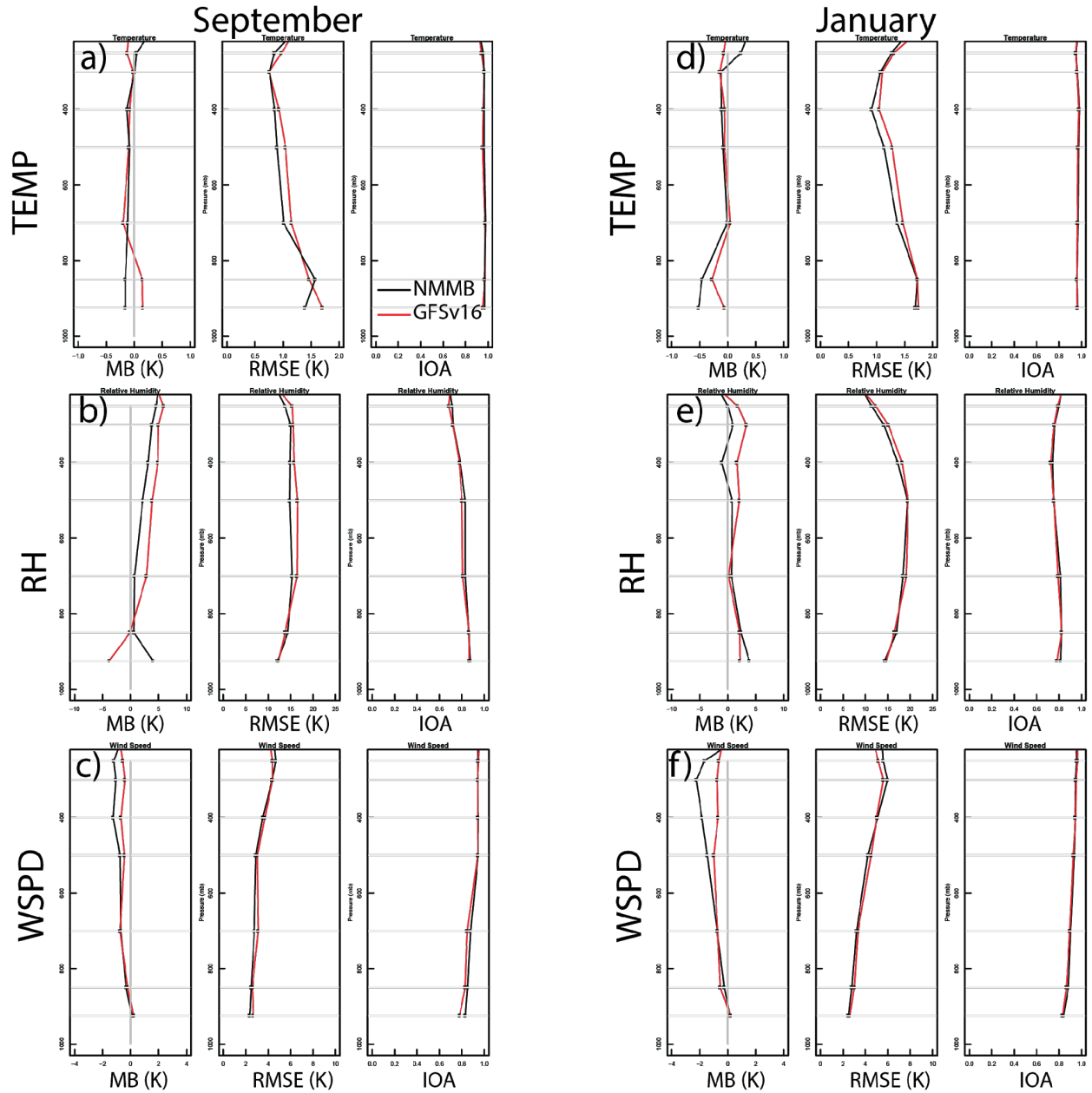
Figure 10. September 2020 (left) and January 2021 (right) vertical (1000 – 250 mb) wind speed (WSPD) statistics (MB, RMSE, and IOA) for NMMB (black) and GFSv16 (red) against an average for select RAOB sites in CONUS. Supporting Figure S15a shows specific RAOB sites, and Supporting Figures S18-S19 provides their relative locations.

4.3 Emissions Analysis

    The updated NEIC2016v1 emissions in NACC-CMAQ are lower compared to the

NEI2014v2 emissions used in the operational NAQFC for all major species, except for NH_3

629   (Table 2), as the NEIC2016v1 includes updated data sources and model projections that

630   projected decreasing emissions compared to the NEI2014v2 (NEIC, 2019).

631   **Table 2.** September and January emissions totals (Tg) for the NAQFC CONUS domain.

Emission Species	NEI2014v2	NEIC2016v1	% Difference
September Total (Tg)			
CO	4.69	4.27	-8.9
NO_x	0.92	0.75	-18.1
SO_2	0.54	0.37	-31.2
NH_3	0.48	0.59	23.9
AVOC	215.58	195.60	-9.3
POC	0.07	0.05	-26.8
PEC	0.03	0.02	-23.9
PMC	2.03	0.82	-59.3
January Total (Tg)			
CO	3.70	3.28	-11.2
NO_x	0.78	0.64	-18.5
SO_2	0.58	0.38	-34.7
NH_3	0.10	0.12	18.4
AVOC	182.02	174.05	-4.4
POC	0.08	0.07	-10.8
PEC	0.02	0.02	-16.7
PMC	1.27	0.24	-80.8

632   Red (blue) shading indicates total emissions increases (decreases).

633

634   The spatial emission changes show widespread decreases in the 2D area/mobile

635   emissions near the major urban cities for CO and NO_x and across the major interstates and

636   railways for NO_x (Figures 11a-b).

637
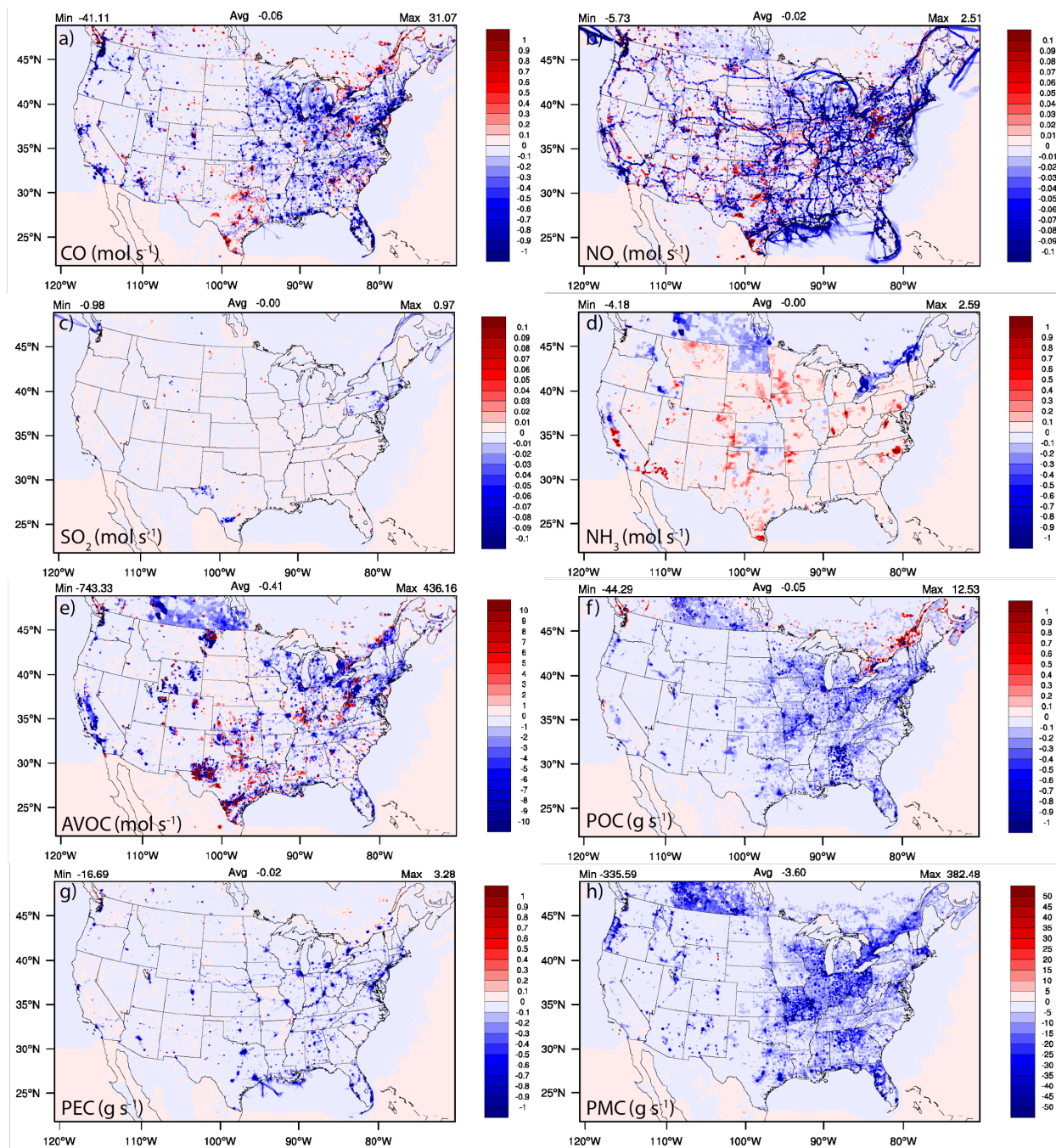
Figure 11. September 2020 average spatial difference plots for NEIC2016v1-NEI2014v2 combined 2D area/mobile emissions. Figure S20 shows very similar emission changes as September, but for January 2021.

The spatial variability in NO_x emission changes, however, are impacted by changes in a number of onroad inputs including vehicles miles traveled, age distribution, and speeds, which caused some emissions to go up or go down depending on the specific counties. The NO_x emissions

646   variability is also impacted by national increases in railway levels and fuel use, while at the same

647   time being impacted by changes to fuel efficiency and cleaner engines for both passenger and

648   commuter trains. There are relatively minor area/mobile changes in SO_2 (Figure 11c), with some

649   exceptions in the east-northeast; however, there are widespread increases in NH_3 emissions

650   driven by changes to the livestock counts and updated fertilization methods and inputs found in

651   the NEIC2016v1 (Figure 11d).   Changes in nonpoint oil and gas production, exploration, and

652   emission factors generation, as well as changes to updated activity and data sources for

653   commercial cooking, residential fuel combustion, and industrial/commercial/institutional (ICI)

654   fuel combustion impact the AVOC area emission changes (Figure 11e). The widespread, and

655   spatially consistent decreases in POC and PMC are due to decreasing fugitive dust sources

656   (Figures 11f and 11h); with the exception of the St. Lawrence River Valley, that has both

657   increases in POC and AVOC (e.g., formaldehyde; not shown) emissions in the NEIC2016v1.

658   Updated appliance counts and residential wood combustion estimates affect the PEC area

659   emission decreases (Figure 11g).

660   There are also biogenic emissions differences due to the updated inline BEISv3.6.1 and

661   BELD5 in NACC-CMAQ (Table 2), and due to the impacts of NMMB (prior NAQFC) vs.

662   GFSv16 (NACC) meteorology on BEIS calculations (Figure 12).
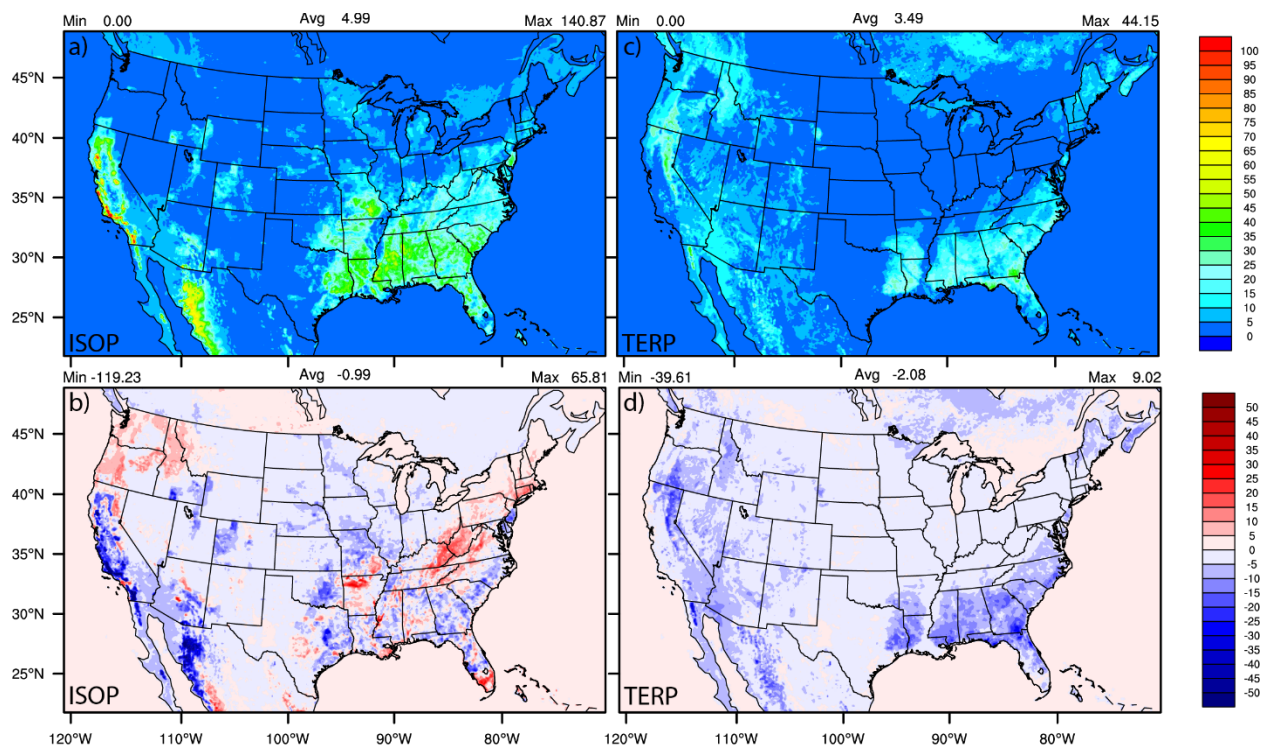
Figure 12. September 2020 average isoprene (ISOP) and terpene (TERP) emissions (top) in the prior NAQFC with BEISv3.1.4, and the absolute differences (bottom) for NACC-CMAQ (with BEISv3.6.1) - NAQFC.

The lower GFSv16 temperatures near many of the highly vegetated regions of the CONUS in September (Figure 4b) decrease the isoprene (ISOP) and terpene (TERP) emissions, with some notable, localized ISOP emission increases due to larger relative increases in downward solar radiation at the surface (GSW; Figure 5b) and resulting Photosynthetic Active Radiation (PAR; not shown). The differences are also impacted by the derivations of leaf temperatures in the updated BEISv3.6.1 and BELD5 in NACC-CMAQ compared to the BEISv3.14 and BELD3 in the prior NAQFC (see discussion in Section 2.2). Hence, the differences in spatial variability between ISOP and TERP emission changes stem from both differences in the locations of their relative maxima, and from the different algorithms for temperature and light dependencies in BEIS. The GFSv16 (NACC) performs very similarly to NMMB (prior NAQFC) for GSW at the surface compared against BSRN-SURFRAD observations in CONUS, with a slightly larger

679 overprediction in the late afternoon at some sites (Figures S21 and S22). The relatively lower

680 ISOP and TERP emissions in NACC-CMAQ will effectively lower the ground-level O_3 and

681 contribution of secondary organic aerosol (SOA) formation to $PM_{2.5}$ compared to the prior

682 NAQFC, particularly in the southeast and parts of the western CONUS in the late summer/early

683 fall. This is somewhat mitigated by enhanced GSW in NACC-CMAQ.

684 4.4 Air Quality Analysis

686   Here we focus on analysis of NACC-CMAQ predictions of gaseous O_3 for the late

687 summer/early fall (September 2020) and $PM_{2.5}$ concentrations during the winter (January 2021)

688 as concentrations are relatively higher for the pollutant's respective seasons. Analysis of NACC-

689 CMAQ gaseous and particulate matter predictions are expanded to other months/seasons in Tang

690 et al. (2022).   During the late U.S. ozone season in September 2020, a large majority of the local

691 NO_x concentration increases in NACC-CMAQ (Figures 13a-b) correlate with areas of NO_x

692 emissions increases in the NEIC2016v1 compared to the NEI2014v2 (Figure 11b). An exception

693 is the large NO_x increases in the far west (e.g., California and Oregon) that stem from gaseous

694 NO_x emissions from strong wildfires that are captured by the GBBEPx in NACC-CMAQ (Table

695 1) but are excluded from the prior NAQFC wildfire emissions system (Table S2). Analyses of

696 the gaseous NO_x emissions effects in NACC-CMAQ is further explored in Tang et al. (2022).

September 2020 Gases
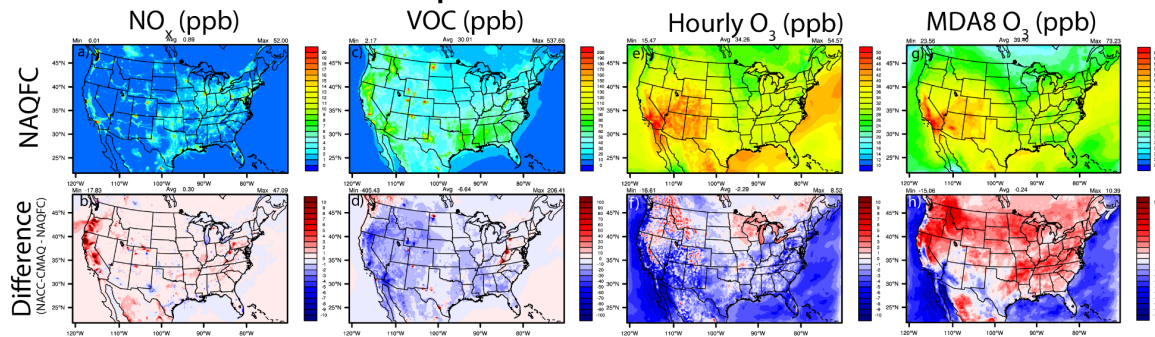
January 2021 Aerosols
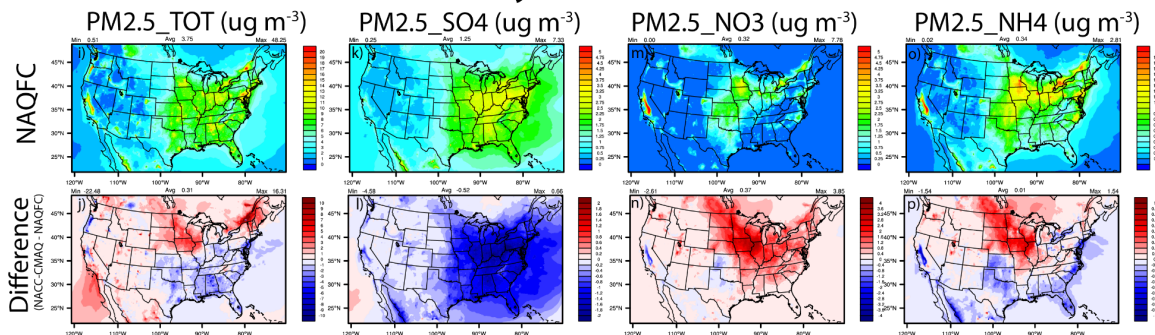
704   The increases in NO_x concentrations and enhanced nighttime O_3 titration, widespread decreases

705   in total VOC concentrations due to both anthropogenic and biogenic VOC emission decreases in

706   NACC-CMAQ, and GFSv16-meteorology effects (e.g., higher PBLH) lead to widespread

707   decreases in hourly O_3 when averaged over all hours (Figures 13e-f). Regions of higher NO_x

708   emissions, overall drier (i.e., widespread lower Q2) conditions, and stronger mid- to late-

709   afternoon solar radiation at the surface (i.e., widespread higher GSW) (see Figures 4-5 and

710   Figures S21-22) lead to enhanced daytime O_3 formation, which is shown in the widespread

711   increases in the maximum daily 8-hr average (MDA8) O_3 for NACC-CMAQ (Figures 13g-h).

712   This is particularly true for the strong NO_x-limited conditions in the western CONUS, where the

713   MDA8 O_3 increases are impacted by large increases in wildfire NO_x emissions in GBBEPx and

714   VOC decreases (anthropogenic+biogenic, but no wildfire VOC emission impacts) in NACC-

715   CMAQ. These effects subsequently impact the ozone NO_x-VOC sensitivity/regime that

716 enhances the NO_x-saturated (i.e., VOC-limited) conditions in this case (Figure S24). There are

717 exceptions with MDA8 O_3 decreases in the west, including western Oregon, the San Joaquin

718 Valley in California, and regions of the southwest CONUS, all of which are strongly VOC-

719 limited (Figure S24). These regions are further impacted by the VOC decreases and further NO_x

720 saturation from wildfire emissions in some locations of the west. We note that Tang et al. (2022)

721 found that the NACC/GFSv16-CMAQ system yields reasonable results when comparing fire-

722 enhanced O_3 and $PM_{2.5}$ concentrations to aircraft measurements during the 2019 Fire Influence

723 on Regional to Global Environments and Air Quality (FIREX-AQ) field campaign

724 (https://csl.noaa.gov/projects/firex-aq/). Further details on the CONUS August-September

725 2019-2020 wildfire emissions impacts on both O_3 and $PM_{2.5}$ in the NACC-CMAQ system are

726 provided in Tang et al. (2022). The widespread decreases in both the hourly and MDA8 O_3

727 over all oceanic regions in the domain are driven by the updated halogen (e.g., bromine and

728 iodine chemistry) mediated O_3 loss in NACC-CMAQ, which can reduce annual mean surface

729 ozone over seawater by 25% (Sarwar et al., 2019).

730 There are both relatively large increases (north, northeast and west) and decreases (south-

731 southeast and parts of the west) for winter (January 2021) total $PM_{2.5}$ (PM25_TOT) in CONUS

732 for NACC-CMAQ compared to NAQFC (Figures 13i-j). The decreases in inorganic

733 PM25_TOT in the east-southeast are dominated by decreases in particulate sulfate (PM25_SO4)

734 and ammonium (PM25_NH4), while the increases in the north-central eastern CONUS are

735 driven by increases in particulate nitrate (PM25_NO3) and PM25_NH4. Further analysis

736 indicates that the widespread decreases in PM25_SO4, most prolifically in the east, are driven

737 strongly by widespread lower CFRAC in GFSv16 (Figure 4o-p) and lower aqueous-phase

738 oxidation in CMAQ (not shown). There are also contributions from decreased SO_2 emissions

739 found in some CONUS regions for NACC-CMAQ (e.g., northeast; Figure 11c). Additional

740 consumption of inorganic sulfate as secondary isoprene epoxydiol (IEPOX) organosulfates are

741 formed in the updated AERO7 aerosol mechanism in NACC-CMAQ (Table 1; Pye et al. 2013,

742 2017), and further contribute to the PM25_SO4 decreases. The higher total PRECIP for NACC-

743 CMAQ (Figure 5) also leads to lower PM25_TOT in the east-southeast regions.

744   The largest PM25_TOT increases in the north-central CONUS are primarily driven by

745 enhanced ammonium nitrate formation, PM25_NO3 and PM25_NH4, which are influenced by

746 increases in NH_3 emissions (Figure 11) and the inclusion of BIDI-NH3 fluxes in NACC-CMAQ

747 (Table 1). BIDI-NH3 in NACC-CMAQ allows for inline calculation of the diurnal pattern of

748 both NH_3 evasion/emission and deposition, while the prior NAQFC only includes deposition.

749 Consequently, BIDI-NH3 in NACC-CMAQ generally increases ambient NH_4^+ and NO_3^- aerosol

750 concentrations (Bash et al., 2013; Pleim et al., 2019) compared to the prior NAQFC.

751   There are also contributions to the increased PM25_TOT from organic carbon sources

752 (Figure S25; PM25_OC), especially in the northeastern portion of the domain that include the St.

753 Lawrence River Valley region. This is in part due to enhanced anthropogenic VOC emissions in

754 NEIC2016v1 (Figure 11e, e.g., formaldehyde; not shown) and more aggressive AERO7

755 secondary organic aerosol formation in this region for NACC-CMAQ (not shown). There are

756 also small PM25_EC contributions to the PM25_TOT decreases in the east and increases in the

757 west for NACC-CMAQ (Figure S25), which are mainly due to decreases in anthropogenic PEC

758 emissions in the east (Figure 11g), but also from contributions of relatively small GBBEPx

759 wildfire PM emissions in the west (not shown). The prior NAQFC does not include wildfire

760 smoke emissions during the month of January.

761

762   4.5 Air Quality Evaluations and Metrics
763

764   Evaluation of NACC-CMAQ shows overall improvement in the spatial MB of hourly O_3

765   (September) and $PM_{2.5}$ (January) against the AirNow network across CONUS (Figure 14).

766   There are clear reductions in the NAQFC overpredictions of O_3 and $PM_{2.5}$ in the east, and overall

767   reduction in NME, and overall improved correlation (R) and IOA for NACC-CMAQ. There are

768   also reduced overpredictions in the west for O_3 in September. The shifts to lower concentrations

769   result in larger domain-wide average $PM_{2.5}$ underpredictions for NACC-CMAQ compared to the

770   prior NAQFC (cf. Figure 13 above); however, *the improvements in R and IOA for NACC-*

771   *CMAQ are substantial*. The MDA8 O_3 spatial MB evaluation against AirNow behaves similarly

772   to NAQFC, with slight degradation in the model performance statistics because of areas of

773   higher overpredictions in the eastern U.S due to reasons discussed above for enhanced daytime

774   O_3 formation in NACC-CMAQ (Figure S26).

Day 1 Mean Bias (Model-AirNow) Plots and Domain-Wide Statistics

a) NAQFC

NMB	23.16
NME	36.34
Corr	0.70
IOA	0.78

Sep 2020: Hourly O_3 (ppb)

b) NACC-CMAQ

NMB	15.28
NME	33.43
Corr	0.72
IOA	0.82

Sep 2020: Hourly O_3 (ppb)

c)

NMB	0.86
NME	65.47
Corr	0.36
IOA	0.58

Jan 2021: Hourly $PM_{2.5}$ ($\mu g\ m^{-3}$)

d)

NMB	-4.79
NME	61.33
Corr	0.41
IOA	0.63

Jan 2021: Hourly $PM_{2.5}$ ($\mu g\ m^{-3}$)

775
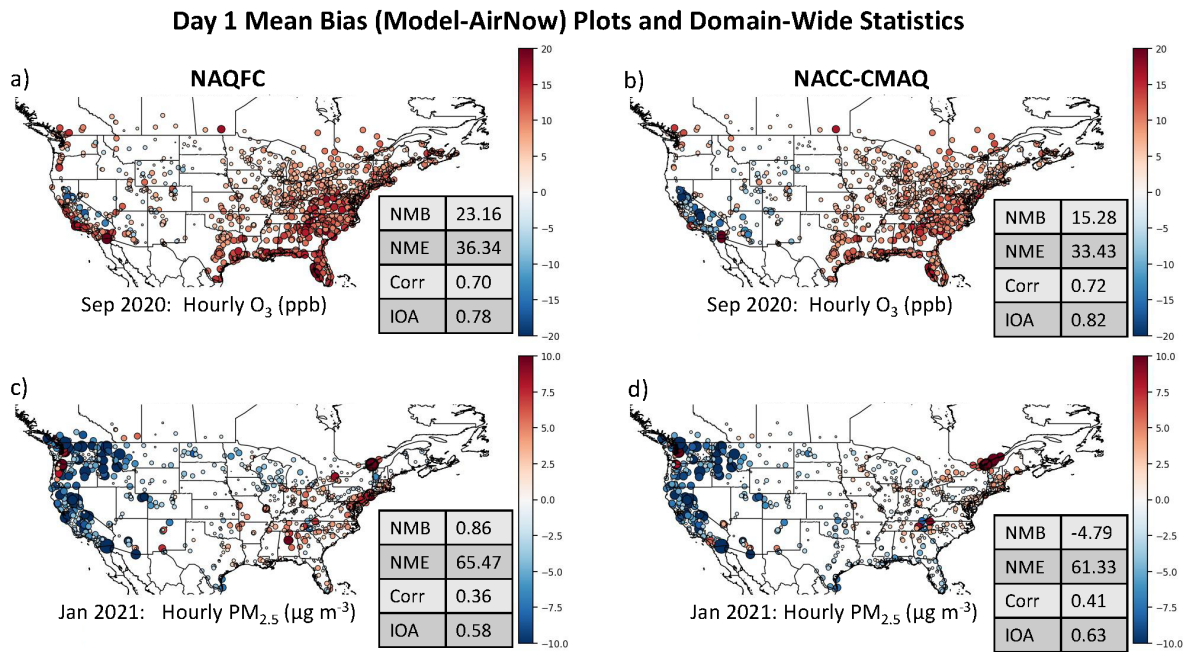
776 **Figure 14.** Day 1 forecast mean bias plots (model-AirNow) for the current operational NAQFC
777 (left) and NACC-CMAQ (right) hourly O_3 (top) and $PM_{2.5}$ (bottom) in a)-b) September 2020 and
778 c)-d) January 2021. Average domain-wide statistics are shown in the tables on the bottom left of
779 each panel.
780
781
782   The Day 2 forecasts have similar spatial model performance and statistics, with improved

783 hourly O_3 and $PM_{2.5}$ model performance (Figure S27) and slightly higher MDA8 O_3

784 overpredictions in the east for NACC-CMAQ (Figure S28). The consistent model performance

785 for Day 3 also shows utility in extending to 72-hr air quality forecasts in the advanced NACC-

786 CMAQ system (Figures S29-30). There is, however, a more notable degradation in skill for the

787 Day 3 forecast of $PM_{2.5}$ compared to O_3 in NACC-CMAQ (compare Figures 14 and S29).

788   There is significant improvement in the average O_3 and $PM_{2.5}$ diurnal patterns for each

789 CONUS region, other than higher daytime O_3 peaks for NACC-CMAQ compared to prior

790 NAQFC (Figure 15a-i). This is reflected in the improved R and IOA over CONUS on average

791 for NACC-CMAQ (Figure 14a-b). There is improved day-to-night O_3 transition, i.e., a sharper

792 slope or cutoff of daytime O_3 formation, which leads to lower nighttime O_3 mixing ratios in

793 NACC-CMAQ that agree better with AirNow observations for all CONUS regions.

794   The NACC-CMAQ $PM_{2.5}$ diurnal pattern also is more consistent with AirNow for most

795 CONUS regions (Figure 15j-s), which is supported by improved R and IOA (Figures 14c-d).

796 There are, however, some regions (e.g., northeast, south, and northwest) that the prior NAQFC

797 shows better diurnal performance in this case.

798
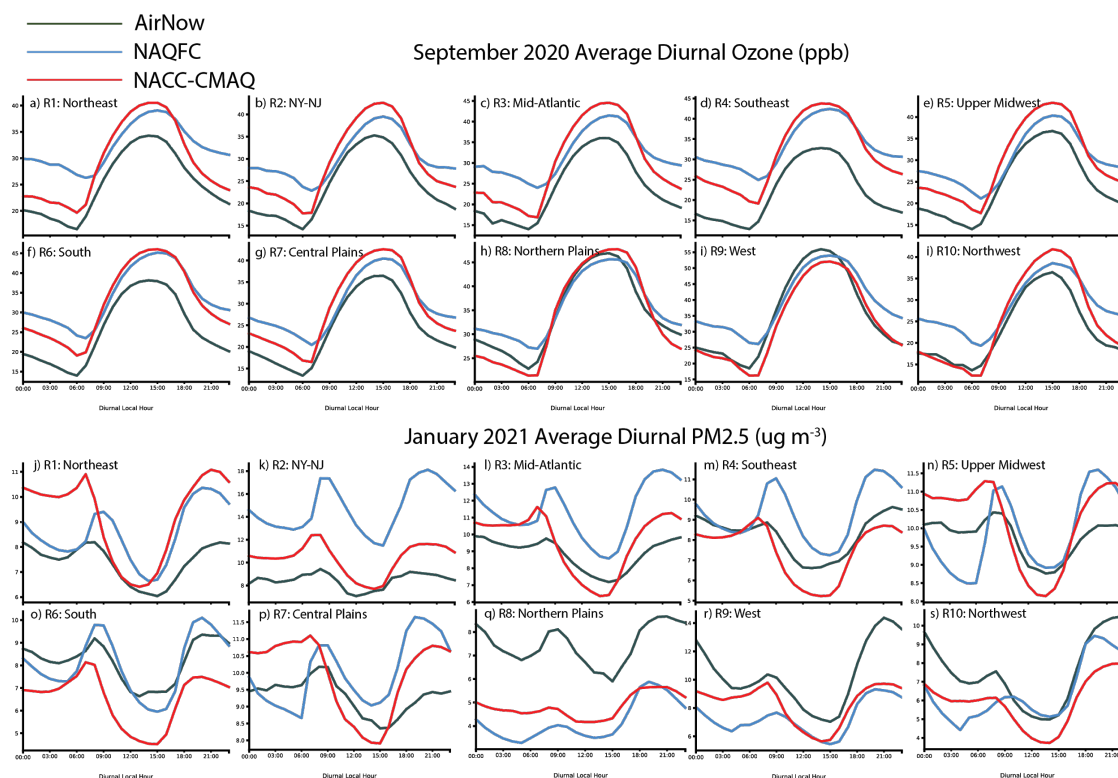
799
800 **Figure 15.** Average September 2020 O_3 (top) and January 2021 $PM_{2.5}$ (bottom) diurnal patterns
801 for NAQFC (blue), NACC-CMAQ (red), and AirNow observations (green) for different regions
802 in CONUS. The regions are based on https://www.epa.gov/aboutepa/regional-and-geographic-
803 offices.

804   Overall performance evaluations of hourly O_3 in each CONUS region show

805 predominantly improved statistics for NACC-CMAQ, with increased R and IOA for all regions

806 (Table 3). Comparisons of the NMB, NME, and R against statistical benchmark values for

807 photochemical models based on Emery et al. (2017) indicate that both the prior NAQFC and

808 NACC-CMAQ are within specified criteria for hourly O_3 in most regions, except for relatively

809 large NMB values in the west and northwest regions. The increased hourly O_3 underpredictions

810 in NACC-CMAQ degrades the NMB to fail to meet the benchmark in the west, but improves the

811 NMB to fall within criteria in the northwest region.

813
814
815
816
817

Table 3. Average September 2020 hourly O$_3$ evaluation of the operational NAQFC and NACC-CMAQ Day 1 forecasts against the AirNow network in different CONUS regions (based on https://www.epa.gov/aboutepa/regional-and-geographic-offices). Statistical benchmark values based on Emery et al. (2017) are also shown for comparison. Following Emery et al., a >40 ppb (i.e., daytime) cutoff for hourly O$_3$ is applied for the mean observations, mean models, mean bias, and the calculated values of NMB and NME, but not for the correlation value (r) or index of agreement (IOA). Total # of obs-model pairs are based on all values (i.e., no cutoff). **Bold** indicates statistical values outside of the Emery et al. criteria. Blue (red) shading indicates improved (degraded) NACC-CMAQ performance. Supporting Tables S5-S10 provide Day 2 and Day 3 (NACC-CMAQ only) forecast evaluations.

Day 1 Forecasts	Total # of Pairs	Mean Obs (ppb)	Mean Mod (ppb)	Mean Bias (ppb)	NMB (%)	NME (%)	Corr (r)	IOA
Benchmark Emery et al. (2017)	-	-	-	-	Goal: <±5% Criteria: <±15%	Goal: <15% Criteria: <25%	Goal: >0.75 Criteria: >0.50	-
Region 1 (Northeast)								
NAQFC	35983	46.85	43.55	-3.31	-7.06	15.04	0.61	0.71
NACC-CMAQ			43.44	-3.42	-7.29	15.14	0.70	0.81
Region 2 (NY-NJ)								
NAQFC	22944	46.68	42.90	-3.77	-8.09	17.88	0.59	0.72
NACC-CMAQ			45.18	-1.50	-3.21	14.27	0.72	0.81
Region 3 (Mid-Atlantic)								
NAQFC	89069	46.66	44.29	-2.37	-5.09	12.84	0.65	0.73
NACC-CMAQ			45.81	-0.85	-1.83	13.48	0.74	0.82
Region 4 (Southeast)								
NAQFC	105858	44.62	45.93	1.31	2.93	13.37	0.61	0.65
NACC-CMAQ			47.99	3.37	7.55	14.91	0.74	0.75
Region 5 (Upper Midwest)								
NAQFC	109744	46.61	43.84	-2.77	-5.94	13.28	0.69	0.77
NACC-CMAQ			46.59	-0.03	-0.05	10.69	0.77	0.83

Region 6 (South)								
NAQFC	84005	48.17	47.18	-0.99	-2.06	13.17	0.68	0.75
NACC-CMAQ			47.81	-0.36	-0.75	12.80	0.75	0.81
Region 7 (Central Plains)								
NAQFC	27139	44.98	44.84	-0.14	-0.31	10.45	0.76	0.81
NACC-CMAQ			47.18	2.20	4.90	9.54	0.82	0.86
Region 8 (Northern Plains)								
NAQFC	51759	48.97	44.64	-4.32	-8.83	13.89	0.71	0.82
NACC-CMAQ			45.08	-3.89	-7.95	14.00	0.72	0.85
Region 9 (West)								
NAQFC	124051	55.44	50.29	-5.15	-9.29	18.37	0.69	0.79
NACC-CMAQ			46.37	-9.07	**-16.37**	21.78	0.71	0.83
Region 10 (Northwest)								
NAQFC	14139	48.41	39.37	-9.03	**-18.66**	21.59	0.61	0.72
NACC-CMAQ			41.70	-6.71	-13.86	19.91	0.66	0.81

827

828   The higher MDA8 O$_3$ in NACC-CMAQ degrades its regional NMB, NME, and R

829 performance slightly compared to the prior NAQFC (Table 4), but R and IOA illustrate

830 improvements for most regions, in some cases substantially for R (e.g., northeast, southeast,

831 upper Midwest, and the Central Plains). The higher daytime O$_3$ overpredictions by NACC-

832 CMAQ in much of CONUS result in higher NMB and NME values that fall outside of the Emery

833 et al. (2017) benchmark criteria. These remain a concern for both the prior NAQFC and NACC-

834 CMAQ, and efforts are underway to address the persistent daytime O$_3$ overprediction in the

835 summer, particularly in the eastern U.S. (see Figures 14a-b and further discussion in Section 5).

836
837
838

Table 4. Same as in Table 3, but for MDA8 O$_3$. Note: As discussed in Emery et al. (2017), cutoff values are not applied for MDA8 O$_3$.

Day 1 Forecasts	Total # of Pairs	Mean Obs (ppb)	Mean Mod (ppb)	Mean Bias (ppb)	NMB (%)	NME (%)	Corr (r)	IOA
Benchmark Emery et al. (2017)	-	-	-	-	Goal: <±5% Criteria: <±15%	Goal: <15% Criteria: <25%	Goal: >0.75 Criteria: >0.50	-
Region 1 (Northeast)								
NAQFC	1680	33.05	38.45	5.40	**16.35**	22.60	0.66	0.73
NACC-CMAQ			38.60	5.55	**16.81**	21.57	0.73	0.75
Region 2 (NY-NJ)								
NAQFC	1158	32.79	37.07	4.29	13.08	21.38	0.66	0.76
NACC-CMAQ			39.22	6.44	**19.63**	23.65	0.74	0.75
Region 3 (Mid-Atlantic)								
NAQFC	4243	33.85	39.35	5.50	**16.24**	20.75	0.74	0.77
NACC-CMAQ			41.31	7.46	**22.05**	24.54	0.76	0.75
Region 4 (Southeast)								
NAQFC	5076	31.01	40.30	9.29	**29.95**	**31.83**	0.64	0.64
NACC-CMAQ			41.06	10.05	**32.41**	**33.40**	0.74	0.67
Region 5 (Upper Midwest)								
NAQFC	5210	34.08	37.88	3.80	11.16	18.51	0.75	0.82
NACC-CMAQ			39.89	5.81	**17.06**	19.94	0.82	0.82
Region 6 (South)								
NAQFC	3901	35.65	42.37	6.72	**18.84**	23.91	0.74	0.77
NACC-CMAQ			43.01	7.35	**20.63**	24.35	0.78	0.78
Region 7 (Central Plains)								

NAQFC	1256	33.37	37.83	4.46	13.36	17.99	0.78	0.82
NACC-CMAQ			39.36	6.00	**17.97**	19.86	0.85	0.84
Region 8 (Northern Plains)								
NAQFC	2379	44.18	43.51	-0.47	-1.07	12.84	0.74	0.85
NACC-CMAQ			44.95	0.78	1.76	11.78	0.79	0.88
Region 9 (West)								
NAQFC	5757	51.03	51.26	0.23	0.44	17.84	0.70	0.82
NACC-CMAQ			48.03	-3.00	-5.88	18.73	0.68	0.79
Region 10 (Northwest)								
NAQFC	698	33.13	35.46	2.33	7.03	**25.11**	0.63	0.72
NACC-CMAQ			36.66	3.53	10.67	**25.58**	0.59	0.74

There are substantial improvements in the overall statistical PM$_{2.5}$ performance for NACC-CMAQ, especially for R and IOA in most CONUS regions.   In many regions where the prior NAQFC falls outside of photochemical criteria values (Emery et al., 2017), NACC-CMAQ shows significant improvement to fall within the criteria. This demonstrates a substantial improvement in the accuracy of the NACC-CMAQ system for PM$_{2.5}$ predictions (outside of major wildfires), attributed to the scientific advancements described above.

856 **Table 5.** Same as in Table 3, but for 24-hr average PM$_{2.5}$. Note: As discussed in Emery et al.
857 (2017), cutoff values are not applied for 24-hr average PM$_{2.5}$.

Day 1 Forecasts	Total # of Pairs	Mean Obs (ppb)	Mean Mod (ppb)	Mean Bias (ppb)	NMB (%)	NME (%)	Corr (r)	IOA
Benchmark Emery et al. (2017)	-	-	-	-	Goal: <±10% Criteria: <±30%	Goal: <35% Criteria: <50%	Goal: >0.70 Criteria: >0.40	-
Region 1 (Northeast)								
NAQFC	1261	7.43	8.47	1.04	13.98	42.57	0.77	0.85
NACC-CMAQ			9.39	1.95	26.30	46.17	0.75	0.83
Region 2 (NY-NJ)								
NAQFC	598	8.54	15.39	6.85	**80.25**	**89.21**	0.72	0.55
NACC-CMAQ			10.84	2.30	26.90	47.60	0.77	0.74
Region 3 (Mid-Atlantic)								
NAQFC	1897	9.16	11.95	2.79	**30.43**	42.57	0.81	0.84
NACC-CMAQ			10.16	1.00	10.96	33.24	0.83	0.89
Region 4 (Southeast)								
NAQFC	3621	8.45	9.67	1.23	14.53	40.44	0.41	0.62
NACC-CMAQ			7.86	-0.59	-6.98	37.19	0.48	0.67
Region 5 (Upper Midwest)								
NAQFC	3270	9.61	9.79	0.19	1.93	38.09	0.58	0.75
NACC-CMAQ			9.65	0.04	0.46	31.42	0.72	0.84
Region 6 (South)								
NAQFC	2101	8.39	7.95	-0.44	-5.19	46.68	**0.28**	0.57
NACC-CMAQ			6.39	-2.00	-23.82	43.30	0.36	0.59
Region 7 (Central Plains)								

NAQFC	926	8.67	9.83	1.16	13.41	49.67	**0.32**	0.58
NACC-CMAQ			8.79	0.12	1.40	32.13	0.68	0.82
Region 8 (Northern Plains)								
NAQFC	1790	7.66	4.36	-3.30	**-43.13**	**60.51**	**0.33**	0.55
NACC-CMAQ			4.89	-2.77	**-36.20**	**52.68**	0.49	0.67
Region 9 (West)								
NAQFC	4118	10.09	7.04	-3.05	**-30.27**	46.97	0.61	0.74
NACC-CMAQ			7.98	-2.11	-20.89	**50.69**	0.56	0.73
Region 10 (Northwest)								
NAQFC	3922	7.93	6.86	-1.07	-13.54	**78.99**	**0.20**	0.46
NACC-CMAQ			6.33	-1.60	-20.19	**71.73**	**0.23**	0.49

858
859
860   The Day 2 forecast comparisons of the prior NAQFC and NACC-CMAQ regional

861 statistics are similar to Day 1, and that the Day 3 forecast extension for NACC-CMAQ has utility

862 with O_3 and $PM_{2.5}$ statistics predominantly falling within the benchmark criteria in most regions

863 (Tables S5-S10).

864 **5. Conclusions and Path Forward**

865   An advanced National Air Quality Forecasting Capability (NAQFC) was developed and

866 evaluated, using NOAA's FV3-based Global Forecast System (GFS) as the driving meteorology

867 for a state-of-the-science Community Multiscale Air Quality (CMAQ) model, version 5.3.1. A

868 key component of this new system is the development of the NOAA-EPA Atmosphere

869 Chemistry Coupler (NACC), which forms the bridge between the GFSv16 meteorological fields

870 and the CMAQ inputs for improved chemical predictions (i.e., NACC-CMAQ).   Such

871 advancements of the NACC-CMAQ system include high-resolution satellite vegetation inputs,

872 with a rapid-refresh VIIRS greenness vegetation fraction and VIIRS climatological leaf area

873   index, as well as additional soil data inputs to an improved windblown dust (FENGSHA)

874   algorithm in CMAQ. The anthropogenic, biogenic, and wildfire emissions in NACC-CMAQ are

875   also updated compared to the prior NAQFC, and for the first time, the forecasting model

876   calculates inline bidirectional NH_3 fluxes. NACC-CMAQ also ingests novel smoke and dust

877   aerosols at its lateral boundaries dynamically from the NOAA operational GEFS-Aerosols

878   model.   Finally, the NACC-CMAQ system extends the air quality forecast from 48 to 72-hours,

879   and provides scientific advances in atmospheric chemistry modeling to state and local forecasters

880   out to 3 days. The additional day of forecast guidance could aid decision makers to prepare

881   citizens for localized air quality conditions that could adversely affect public health.

882   Results of the NACC-CMAQ system during recent late summer (September 2020) and

883   winter (January 2021) months show significant changes in both meteorological and chemical

884   predictions compared to the prior NAQFC. The GFSv16 for NACC-CMAQ has a persistently

885   large dry bias (lower Q2) and larger RMSE across much of CONUS in late summer compared to

886   NMMB (i.e., prior NAQFC), which likely stems from excessively dry soil conditions in GFS.

887   GFS is generally cooler in the east and warmer in the west for surface temperature (TEMP2)

888   compared to NMMB, but the overall MB and RMSE are more similar between the models

889   compared to that for Q2. The GFS has a relatively similar planetary boundary layer height

890   (PBLH) at night, but the PBLH in GFSv16 (NACC-CMAQ) is consistently deeper during the

891   daytime peak hours compared to the prior NAQFC. The differences in surface characteristics,

892   meteorology, and both anthropogenic and natural emissions are driving factors for distinct

893   atmospheric composition differences, where NACC-CMAQ generally outperforms the prior

894   NAQFC for both hourly O_3 and $PM_{2.5}$, especially with improved correlation (R) and IOA. This

895   agrees well with significant improvements in the diurnal O_3 and $PM_{2.5}$ patterns for NACC-

896   CMAQ, with distinct improvements in the day-to-night O_3 slope/cutoff. While overall similar,

897   the maximum daily 8-hr average (MDA8) O_3 is predominantly higher for NACC-CMAQ

898   compared to prior NAQFC, which leads to some forecast degradation due to larger

899   overpredictions of the daytime max O_3.

900   The NACC-CMAQ became the next operational version of the NAQFC at NWS/NOAA

901   on July 20, 2021, and is available on GitHub for continuous integration, future code updates, and

902   potential community research applications. A comparison and evaluation of the GFSv16/NACC-

903   CMAQ output with a GFSv16-downscaled Weather Research and Forecasting (WRF) Version 4

904   (Skamarock et al., 2019) and CMAQ application serves to highlight the potential of NACC-

905   CMAQ as an additional community research tool for air quality applications (Tang et al., 2022).

906   While there are substantial advancements in NACC-CMAQ compared to the prior

907   NAQFC, challenges and limitations remain. One need is to bridge the gap from using a VIIRS

908   LAI climatology to a rapid-refresh, i.e., dynamic methodology (similar to the GVF method here)

909   in NACC-CMAQ. There is also a need to consider shifting the paradigm from using "big-leaf"

910   (i.e., homogeneous single layer of phytomass) assumptions that strongly affect the biosphere-

911   atmosphere exchange processes pivotal to both meteorological and chemical model predictions

912   (refer to Bonan et al., 2021). Simple multilayer canopies have shown to reduce overpredictions

913   of ground-level surface O_3 in the summer due to photolysis attenuation and modified vertical

914   turbulence (Makar et al., 2017), which have significant implications for the daytime O_3

915   overpredictions in the current and future versions of NAQFC (Figures 14a-b and S26). We are

916   currently working on similar canopy effects in NACC-CMAQ to reduce the summer O_3

917   overpredictions in the east-southeast and parts of western CONUS where there are relatively

918   continuous vegetation/canopies (Figures 14a-b). Other advancements that are important to

919 improving the future versions of the NAQFC include dynamically updated (and weather-

920 dependent) anthropogenic emissions sources, and improved treatments of mobile sources (e.g.,

921 Vehicle Induced Turbulence; Makar et al., 2021). Further refinements to the inline windblown

922 dust emissions, wildfire smoke emissions, and other process-based natural emissions sources are

923 also needed.

924   Other future directions including migrating the advanced science in the offline 12 km

925 resolution NACC-CMAQ model, to a next-generation inline, high-resolution (e.g., 3 km)

926 modeling framework that fits within NOAA's strategy for the Unified Forecast System (UFS;

927 https://ufscommunity.org/). This model system aims to improve integration of atmospheric

928 composition changes with weather predictions, better resolve finer scale processes, and advance

929 the rapid-refresh techniques for emissions and surface-atmosphere exchange processes. The

930 advanced NACC-CMAQ system is an important step to advance the NAQFC closer to the state-

931 of-the-science for regional air quality forecasting, improves community applications of NOAA's

932 FV3GFS-driven atmospheric composition models, and facilitates future development of inline,

933 regional high-resolution air quality forecasting systems within the UFS framework.

934 **Code and Data Availability**

935   The NACC code is publicly available at https://doi.org/10.5281/zenodo.5507489 and via

936 GitHub at https://github.com/noaa-oar-arl/NACC.git. The modified version of CMAQv5.3.1

937 used in the advanced NACC-CMAQ model for the next operational NAQFC is available at

938 https://doi.org/10.5281/zenodo.5507511 and via GitHub at https://github.com/noaa-oar-

939 arl/NAQFC-WCOSS.

940   The 0.25 degree FV3-driven Global Forecast System Version 16 data (cycled 4x/day) is

941 available in GRIB2 format at https://www.nco.ncep.noaa.gov/pmb/products/gfs/. The hourly

942 GFSv16 data in gridded NetCDF (~13x13 km globally) format and Gaussian projection that is

943 directly used to drive NACC-CMAQ is currently being migrated to Amazon Web Services

944 (AWS) Cloud for improved NOAA community air quality research applications. The advanced

945 NACC-CMAQ data, i.e., the current operational NAQFC version as of July 2021, is available for

946 operational (https://airquality.weather.gov/) and interactive

947 (https://digital.mdl.nws.noaa.gov/airquality/#) displays from NWS/NOAA. The official

948 NOAA/EMC verification and diagnostics for the NAQFC system are found at

949 https://www.emc.ncep.noaa.gov/mmb/aq/verification_diagnostics/cmaq_verf/.

Disclaimer

951 The scientific results and conclusions, as well as any views or opinions expressed herein,

952 are those of the author(s) and do not necessarily reflect the views of NOAA or the Department of

953 Commerce. The research presented was not funded by EPA and was not subject to EPA's quality

954 system requirements. The views expressed in this article are those of the author(s) and do not

955 necessarily represent the views or the policies of the U.S. Environmental Protection Agency.

Author Contribution

957 Patrick C. Campbell: Conceptualization, Methodology, Software, Data curation,

958 Visualization, Investigation, Writing – original draft. Youhua Tang: Methodology, Software,

959 Data curation, Investigation. Pius Lee: Supervision, Project administration, Funding acquisition.

960 Barry Baker: Methodology, Software, Data curation. Daniel Tong: Methodology, Software,

961 Writing – review & editing, Project administration, Funding acquisition. Rick Saylor:

962 Supervision, Project administration, Funding acquisition, Writing – review & editing. Ariel

963 Stein: Supervision, Project administration, Funding acquisition. Jianping Huang: Software, Data

964 curation. Ho-Chun Huang: Methodology, Software, Data curation. Jeff McQueen: Project

965 administration, Funding acquisition. Li Pan: Software, Data curation. Edward Strobach:

966 Software, Data curation, Writing – review & editing. Ivanka Stajner: Project administration,

967 Funding acquisition. Jamese Sims: Project administration. Jose Tirado-Delgado: Project

968 administration. Youngsun Jung: Project administration, Funding acquisition. Fanglin Yang:

969 Project administration. Tanya Spero: Methodology, Software, Writing – review & editing.

970 Robert Gilliam: Software, Data curation.

971 **Declaration of competing interest**

972 The authors declare that they have no known competing financial interests or personal

973 relationships that could have appeared to influence the work reported in this paper.

974 **Acknowledgments**

975 This study was co-funded by the National Oceanic and Atmospheric Administration, the

976 University of Maryland, and George Mason University under the Cooperative Institute for

977 Satellite Earth System Studies (CISESS).

References

Alexander, B., R.J. Park, D.J. Jacob, and S. Gong (2009), Transition metal-catalyzed oxidation of atmospheric sulfur: global implications for the sulfur budget, J. Geophys. Res., 114, D02309, doi: 10.1029/2008JD010486.

Aligo, E., , Ferrier B. S. , , Rogers E. , , Pyle M. , , Weiss S. J. , , and Jirak I. L. , 2014: Modified microphysics for use in high-resolution NAM forecasts. Proc. 27th Conf. on Severe Local Storms, Madison, WI, Amer. Meteor. Soc., 16A.1. [Available online at https://ams.confex.com/ams/27SLS/webprogram/Paper255732.html.]

American Lung Association. Urban air pollution and health inequities: A workshop report. Environ Health Perspect. 2001; 109 (suppl 3): 357-374

Appel, K. W., R.C. Gilliam, N. Davis, A. Zubrow, S.C. Howard Overview of the atmospheric model evaluation tool (amet) v1.1 for evaluating meteorological and air quality models Environ. Model. Software, 26 (2011), pp. 434-443, 10.1016/j.envsoft.2010.09.007

Appel, K. W., Bash, J. O., Fahey, K. M., Foley, K. M., Gilliam, R. C., Hogrefe, C., Hutzell, W. T., Kang, D., Mathur, R., Murphy, B. N., Napelenok, S. L., Nolte, C. G., Pleim, J. E., Pouliot, G. A., Pye, H. O. T., Ran, L., Roselle, S. J., Sarwar, G., Schwede, D. B., Sidi, F. I., Spero, T. L., and Wong, D. C.: The Community Multiscale Air Quality (CMAQ) Model Versions 5.3 and 5.3.1: System Updates and Evaluation (2021), Geosci. Model Dev. Discuss, https://doi.org/10.5194/gmd-14-2867-2021.

Astitha, M., H. Luo, S.T. Rao, C. Hogrefe, R. Mathur, N. Kumar Dynamic evaluation of two decades of WRF-CMAQ ozone simulations over the contiguous United States Atmos. Environ., 164 (2017), pp. 102-116, 10.1016/j.atmosenv.2017.05.020

Bai L, Wang J, Ma X, Lu H. Air Pollution Forecasts: An Overview. Int J Environ Res Public Health. 2018;15(4):780. Published 2018 Apr 17. doi:10.3390/ijerph15040780

Baker, Barry; Pan, Li. 2017. "Overview of the Model and Observation Evaluation Toolkit (MONET) Version 1.0 for Evaluating Atmospheric Transport Models." Atmosphere 8, no. 11: 210. https://doi.org/10.3390/atmos8110210.

Bash, J. O., J. T. Walker, G. G. Katul, M. R. Jones, E. Nemitz, and W. P. Robarge (2010), Estimation of In-Canopy Ammonia Sources and Sinks in a Fertilized Zea mays Field, Environ. Sci. Technol., 44, 1683–1689, doi: 10.1021/es9037269.

Bash, J. O., Cooter, E. J., Dennis, R. L., Walker, J. T., & Pleim, J. E. (2013). Evaluation of a regional air-quality model with bidirectional NH3 exchange coupled to an agroecosystem model. Biogeosciences, 10(3), 1635–1645. https://doi.org/10.5194/bg-10-1635-2013

Bash, J.O., Baker, K.R., Beaver, M.R., 2015, Evaluation of improved land use and canopy representation in BEIS v3.61 with biogenic VOC measurements in California, Geosci. Model Dev. Discuss. 8, 8117-8154, doi:10.5194/gmdd-8-8117-2015

Binkowski, F. S., and Roselle S. J., 2003: Models-3 Community Multiscale Air Quality (CMAQ) model aerosol component 1. Model description. J. Geophys. Res., 108, 4183, doi:10.1029/2001JD001409.

Binkowski, F.S, S. Arunachalam, Z. Adelman, and J. Pinto (2007), Examining photolysis rates with a prototype on-line photolysis module in CMAQ, J. Appl. Meteor. and Clim. 46, 1252-1256, doi: 10.1175/JAM2531.1.

Black, 1994 T. Black The new NMC meso-scale Eta Model: description and forecast examples Weather and Forecasting, 9 (1994), pp. 265-278

Bonan, G. B., E. G. Patton, J. J. Finnigan, D. D. Baldocchi, and I. N. Harman (2021). Moving beyond the incorrect but useful paradigm: reevaluating big-leaf and multilayer plant canopies to model biosphere-atmosphere fluxes – a review. Agricultural and Forest Meteorology. 306. https://doi.org/10.1016/j.agrformet.2021.108435.

Briggs, G. A., "A plume rise model compared with observations," J.A.P.C.A., 15 (9), 433-438 (1965).

Byun and Ching, 1999 Byun, D.W., Ching, J.K.S., (Eds.), 1999. Science algorithms of the EPA Models-3 Community Multi-scale Air Quality (CMAQ) modeling system, EPA/600/R-99/030, Office of Research and Development, US Environmental Protection Agency.

Byun, D., & Schere, K. L. (2006). Review of the governing equations, computational algorithms, and other components of the models-3 community multiscale air quality (CMAQ) modeling system. Applied Mechanics Reviews, 59(1–6), 51–77. https://doi.org/10.1115/1.2128636

Campbell, G. S. and Norman, J. M.: An introduction to environmental biophysics, Springer, 5 1998

Campbell, P., Y. Zhang, K. Yahya, K. Wang, C. Hogrefe, G. Pouliot, C. Knote, A. Hodzic, R. San Jose, J. Perez, P. J. Guerrero, R. Baro, and P. Makar, 2015, A Multi-Model Assessment for the 2006 and 2010 Simulations under the Air Quality Model Evaluation International Initiative (AQMEII) Phase 2 over North America: Part I. Indicators of the Sensitivity of O3 and PM2.5 Formation Regimes, Atmospheric Environment, 115, 569 – 586, doi: 10.1016/j.atmosenv.2014.12.026.

Campbell, P. C., Bash, J. O., & Spero, T. L. (2019). Updates to the Noah land surface model in WRF-CMAQ to improve simulated meteorology, air quality, and deposition. Journal of Advances in Modeling Earth Systems, 11, 231–256. https://doi.org/10.1029/2018MS001422

Campbell, P. C., Tong, D., Tang, Y., Baker, B., Lee, P., Saylor, R., Stein, A., Ma, S., Lamsal, L., and Qu, Z. (2021). Impacts of the COVID-19 Economic Slowdown on Ozone Pollution in the U.S. Atmospheric Environment, In press. Available online 4 September 2021, 118713

J.-H Chen and S.-J Lin. The remarkable predictability of inter-annual variability of atlantic hurricanes during the past decade. Geophysical Research Letters, 38(L11804):6, 2011.

J-H. Chen and S-J. Lin. Seasonal predictions of tropical cyclones using a 25-km-resolution general circulation model. J. Climate, 26(2):380–398, 2013.

Chen, F., & Dudhia, J. (2001). Coupling an advanced land surface-hydrology model with the Penn State-NCAR MM5 modeling system. Part I: Model implementation and sensitivity.

Monthly Weather Review, 129(4), 569–585. https://doi.org/10.1175/1520-0493(2001)129<0569: CAALSH>2.0.CO;2

Chen, X., N. Andronova, B. Van Leer, J.E. Penner, J.P. Boyd, C. Jablonowski, and S. Lin, 2013: A Control-Volume Model of the Compressible Euler Equations with a Vertical Lagrangian Coordinate. Mon. Wea. Rev., 141, 2526–2544, https://doi.org/10.1175/MWR-D-12-00129.1

Chen, Jan-Huey, Xi Chen, Shian-Jiann Lin, Linus Magnusson, Morris A. Bender, Linjiong Zhou and Shannon L. Rees. "TROPICAL CYCLONES IN GFDL FVGFS – IMPACTS OF DYCORE , PHYSICS , AND INITIAL CONDITIONS." (2018).

Chen, X. et al. (2021). Evaluation of the offline-coupled GFSv15-FV3-CMAQv5.0.2 in support of the next-generation National Air Quality Forecast Capability over the contiguous United States. GMD Discussion. Under review.

Chin, M., P. Ginoux, S. Kinne, B. N. Holben, B. N. Duncan, R. V. Martin, J. A. Logan, A. Higurashi, and T. Nakajima, Tropospheric aerosol optical thickness from the GOCART model and comparisons with satellite and sun photometer measurements, J. Atmos. Sci. 59, 461-483, 2002.

Chin, M., R. B. Rood, S.-J. Lin, J. F. Muller, and A. M. Thomspon, Atmospheric sulfur cycle in the global model GOCART: Model description and global properties, J. Geophys. Res., 105, 24,671-24,687, 2000.

Chinese State Council, Air Pollution Prevention and Control Action Plan (Guo Fa [2013] No. 37, Sept. 10, 2013), http://www.gov.cn/zwgk/2013-09/12/content_2486773.htm (in Chinese), archived at https://perma.cc/63LS-QXDJ; English translation at http://en.cleanairchina.org/file/loadFile/26.html, archived at https://perma.cc/S5FB-4ECZ.

Clough, S. A., Shephard, M. W., Mlawer, J. E., Delamere, J. S., Iacono, M. J., Cady-Pereira, K., et al. (2005). Atmospheric radiative transfer modeling: A summary of the AER codes. Journal of Quantitative Spectroscopy & Radiative Transfer, 91(2), 233–244. https://doi.org/10.1016/j.jqsrt.2004.05.058

Cooter, E. J., Bash, J. O., Walker, J. T., Jones, M. R., & Robarge, W. (2010). Estimation of NH3 bi-directional flux from managed agricultural soils. Atmospheric Environment, 44(17), 2107–2115. https://doi.org/10.1016/j.atmosenv.2010.02.044

Cooter, E. J., Bash, J. O., Benson, V., & Ran, L. (2012). Linking agricultural crop management and air quality models for regional to national-scale nitrogen assessments. Biogeosciences, 9(10), 4023–4035. https://doi.org/10.5194/bg-9-4023-2012

Demetriou, C. A., and Vineis, P. (2015). Carcinogenicity of ambient air pollution: use of biomarkers, lessons learnt and future directions.

Ding, H. and Y. Zhu (2018). NDE Vegetation Products System Algorithm Theoretical Basis Document. Version 4.0. NOAA/NESDIS/OSPO. Accessed on February 02, 2021. Available from: https://www.ospo.noaa.gov/Products/documents/GVF_ATBD_V4.0.pdf

Dong, X., J. S. Fu, K. Huang, D. Tong, and G. Zhuang (2016). Model development of dust emission and heterogeneous chemistry within the Community Multiscale Air Quality modeling system and its application over East Asia. Atmos. Chem. Phys., 16, 8157-8180.

Driemel, A., Augustine, J., Behrens, K., Colle, S., Cox, C., Cuevas-Agulló, E., et al. (2018). Baseline Surface Radiation Network (BSRN): Structure and data description (1992–2017). Earth System Science Data, 10(3), 1491–1501. https://doi.org/10.5194/essd-10-1491-2018

Eder, B., Kang, D., Mathur, R., Yu, S., & Schere, K. (2006). An operational evaluation of the Eta-CMAQ air quality forecast model. Atmospheric Environment, 40(26), 4894–4905. https://doi.org/10.1016/j.atmosenv.2005.12.062

Eder, B., Kang, D., Mathur, R., Pleim, J., Yu, S., Otte, T., & Pouliot, G. (2009). A performance evaluation of the National Air Quality Forecast Capability for the summer of 2007. Atmospheric Environment, 43(14), 2312–2320. https://doi.org/10.1016/j.atmosenv.2009.01.033

Ek, M. B., Mitchell, K. E., Lin, Y., Rogers, E., Grunmann, P., Koren, V., et al. (2003). Implementation of Noah land surface model advances in the National Centers for Environmental Prediction operational mesoscale Eta model. Journal of Geophysical Research, 108(D22), 8851. https://doi.org/10.1029/2002JD003296

Emery, C., Zhen Liu, Armistead G. Russell, M. Talat Odman, Greg Yarwood & Naresh Kumar (2017). Recommendations on statistics and benchmarks to assess photochemical model performance, Journal of the Air & Waste Management Association, 67:5, 582-598, DOI: 10.1080/10962247.2016.1265027.

Finkelstein et al. Relation between income, air pollution and mortality: A cohort study. CMAJ. 2003; 169: 397-402

Ginoux, P., M. Chin, I. Tegen, J. Prospero, B. Holben, O. Dubovik, and S.-J. Lin, Sources and global distributions of dust aerosols simulated with the GOCART model, J. Geophys. Res., 106, 20,255-20,273, 2001.

Grell, G. A., Dudhia, J., & Stauffer, D. R. (1994). A description of the fifth-generation Penn State/NCAR Mesoscale Model (MM5). NCAR tech. Note NCAR TN-398-1-STR, 117 pp.

Han, J. and H.-L. Pan, 2011: Revision of Convection and Vertical Diffusion Schemes in the NCEP Global Forecast System. Wea. and Forecasting, 26, 520-533.

Han, J., W. Wang, Y. C. Kwon, S.-Y. Hong, V. Tallapragada, and F. Yang, 2017: Updates in the NCEP GFS Cumulus Convection Schemes with Scale and Aerosol Awareness. Wea. and Forecasting, 32, 2005-2017.

Han, J., & Bretherton, C. S. (2019). TKE-Based Moist Eddy-Diffusivity Mass-Flux (EDMF) Parameterization for Vertical Turbulent Mixing, Weather and Forecasting, 34(4), 869-886.

Harris, L.M. and S. Lin, 2013: A Two-Way Nested Global-Regional Dynamical Core on the Cubed-Sphere Grid. Mon. Wea. Rev., 141, 283–306, https://doi.org/10.1175/MWR-D-11-00201.1

Harris, L.M., S. Lin, and C. Tu, 2016: High-Resolution Climate Simulations Using GFDL HiRAM with a Stretched Global Grid. J. Climate, 29, 4293–4314, https://doi.org/10.1175/JCLI-D-15-0389.1

Hengl, T., Mendes de Jesus, J., Heuvelink, G. B. M., Ruiperez Gonzalez, M., Kilibarda, M., Blagotić, A., Shangguan, W., Wright, M. N., Geng, X., Bauer-Marschallinger, B., Guevara, M. A., Vargas, R., MacMillan, R. A., Batjes, N. H., Leenaars, J. G. B., Ribeiro, E., Wheeler, I., Mantel, S., and Kempen, B.: SoilGrids250m: Global gridded soil information based on machine learning, PLoS ONE, 12, e0169748, http://dx.doi.org/10.1371/journal.pone.0169748, 2017b. Huang, J., J. McQueen, J. Wilczak, I. Djalalova, I. Stajner, P. Shafran, D. Allured, P. Lee, L. Pan, D. Tong, H. Huang, G. DiMego, S. Upadhayay, and L. Delle Monache, 2017: Improving NOAA NAQFC PM2.5 Predictions with a Bias Correction Approach. Wea. Forecasting, 32, 407–421, https://doi.org/10.1175/WAF-D-16-0118.1

Huang, J., J. McQueen, et al., Impact of global scale FV3 versus regional scale NAM meteorological driver model predictions on regional air quality forecasting. The 100th AGU Fall Meeting, December 9-13, 2019, San Francisco, CA.

Huang, J., J. McQueen, et al., Development and evaluation of offline coupling of FV3-based GFS with CMAQ at NOAA, the 17th CMAS Conference, October 22-24, 2018, UNC-Chapel Hill, NC.

Huang. J., J. McQueen, et al., Development and evaluations of the GFS-driven National Air Quality Forecasting Capability at NOAA (in prep, to be submitted to GMD).

Huang, M., and Coauthors, 2015: Toward enhanced capability for detecting and predicting dust events in the western United States: The Arizona case study. Atmos. Chem. Phys., 15, 12 595–12 610, doi:10.5194/acp-15-12595-2015.

Iacono, M. J., Delamere, J. S., Mlawer, E. J., Shephard, M. W., Clough, S. A., & Collins, W. D. (2008). Radiative forcing by long-lived greenhouse gases: Calculations with the AER radiative transfer models. Journal of Geophysical Research, 113, D13103. https://doi.org/10.1029/2008JD009944

Institute of Medicine. Toward Environmental Justice: Research, Education, and Health Policy Needs. Washington, DC: National Academy Press, 1999;

Janjić, Z. I., 2000: Comments on "Development and evaluation of a convection scheme for use in climate models." J. Atmos. Sci., 57, 3686, doi:10.1175/1520-0469(2000)057<3686:CODAEO>2.0.CO;2.

Janjić, Z. I., Gerrity J. P. Jr., and Nickovic S. (2001): An alternative approach to nonhydrostatic modeling. Mon. Wea. Rev., 129, 1164–1178, doi:10.1175/1520-0493(2001)129<1164:AAATNM>2.0.CO;2.

Janjic, Z., & Gall, R. L. (2012). Scientific documentation of the NCEP nonhydrostatic multiscale model on the B grid (NMMB). Part 1 Dynamics (No. NCAR/TN-489+STR). University Corporation for Atmospheric Research. doi: 10.5065/D6WH2MZX.

Jimenez, P. A., Dudhia, J., Gonzalez-Rouco, J. F., Navarro, J., Montavez, J. P., & Garcia-Bustamante, E. (2012). A revised scheme for the WRF surface layer formulation. Monthly Weather Review, 140(3), 898–918. https://doi.org/10.1175/MWR-D-11-00056.1

Kang, Daiwen, Eder, B. K., Stein, A. F., Grell, G. A., Peckham, S. E., & Mc Henry, J. (2005). The New England Air Quality Forecasting Pilot Program: Development of an Evaluation Protocol and Performance Benchmark. Journal of the Air and Waste Management Association, 55(12), 1782–1796. https://doi.org/10.1080/10473289.2005.10464775

Karamchandani, P., Long, Y., Pirovano, G., Balzarini, A., and Yarwood, G.: Source-sector contributions to European ozone and fine PM in 2010 using AQMEII modeling data, Atmos. Chem. Phys., 17, 5643–5664, https://doi.org/10.5194/acp-17-5643-2017, 2017.

Kar Kurt, O., Zhang, J., and Pinkerton, K. E. (2016) Pulmonary Health Effects of Air Pollution. Curr Opin Pulm Med, 22 (2), 138-143. doi:10.1097/MCP.0000000000000248

Kelly, J. T., P. V. Bhave, C. G. Nolte, U. Shankar, and K. M. Foley (2010), Simulating emission and chemical evolution of coarse sea-salt particles in the Community Multiscale Air Quality (CMAQ) model, Geosci. Model Dev., 3, 257–273, doi: 10.5194/gmd-3-257-2010.

Kim, Y., Sartelet, K., Seigneur, C., 2011a. Formation of secondary aerosols: impact of the gas-phase chemical mechanism. Atmos. Chem. Phys. 11, 583e598. http://dx.doi.org/10.5194/acp-11-583-2011.

Kim, Y., Couvidat, F., Sartelet, K., Seigneur, C., 2011b. Comparison of different gas phase mechanisms and aerosol modules for simulating particulate matter formation. J. Air Waste Manag. Assoc. 61, 1218e1226. http://dx.doi.org/10.1080/10473289.2011.603999.

Keller, C. A. and Evans, M. J.: Application of random forest regression to the calculation of gas-phase chemistry within the GEOS-Chem chemistry model v10, Geosci. Model Dev., 12, 1209–1225, https://doi.org/10.5194/gmd-12-1209-2019, 2019.

S.K. Krueger, Q. Fu, K. N. Liou, and H-N. S. Chin. Improvement of an ice-phase microphysics parameterization for use in numerical simulations of tropical convection. Journal of Applied Meteorology, 34:281–287, January 1995.

Landrigan, P. J., et al. (2018). The Lancet Commission on pollution and health. Lancet 2018; 391: 462-512. http://dx.doi.org/10.1016/S0140-6736(17)32345-0

Lee, B.-J., Kim, B., and Lee, K. (2014). Air Pollution Exposure and Cardiovascular Disease. Toxicol Res., 30(2), 71-75.

Lee, P., McQueen, J., Stajner, I., Huang, J., Pan, L., Tong, D., et al. (2017). NAQFC Developmental Forecast Guidance for Fine Particulate Matter (PM 2.5). Weather and Forecasting, 32(1), 343–360. https://doi.org/10.1175/waf-d-15-0163.1

Lin, S., 2004: A "Vertically Lagrangian" Finite-Volume Dynamical Core for Global Models. Mon. Wea. Rev., 132, 2293–2307, https://doi.org/10.1175/1520-0493(2004)132<2293:AVLFDC>2.0.CO;2

Lin, S. and R.B. Rood, 1996: Multidimensional Flux-Form Semi-Lagrangian Transport Schemes. Mon. Wea. Rev., 124, 2046–2070, https://doi.org/10.1175/1520-0493(1996)124<2046:MFFSLT>2.0.CO;2

Y.-L. Lin, R. D. Farley, and H. D. Orville. Bulk parameterization of the snow field in a cloud model. J. Climate Appl. Meteor., 22:1065–1092, 1983.

Lin, S., W.C. Chao, Y.C. Sud, and G.K. Walker, 1994: A Class of the van Leer-type Transport Schemes and Its Application to the Moisture Transport in a General Circulation Model. Mon. Wea. Rev., 122, 1575–1593, https://doi.org/10.1175/1520-0493(1994)122<1575:ACOTVL>2.0.CO;2

Liu, Y. and Wang, T.: Worsening urban ozone pollution in China from 2013 to 2017 – Part 1: The complex and varying roles of meteorology, Atmos. Chem. Phys., 20, 6305–6321, https://doi.org/10.5194/acp-20-6305-2020, 2020.

S.J. Lord, H.E. Willoughby, and J.M. Piotrowicz. Role of a parameterized ice-phase microphysics in an axisymmetric, nonhydrostatic tropical cyclone model. J. Atmos. Sci., 41(19):2836–2848, October 1984.

Makar, P., Staebler, R., Akingunola, A. et al. The effects of forest canopy shading and turbulence on boundary layer ozone. Nat Commun 8, 15243 (2017). https://doi.org/10.1038/ncomms15243

Makar, P. A., Stroud, C., Akingunola, A., Zhang, J., Ren, S., Cheung, P., and Zheng, Q.: Vehicle-induced turbulence and atmospheric pollution, Atmos. Chem. Phys., 21, 12291–12316, https://doi.org/10.5194/acp-21-12291-2021, 2021

Marlier, M.E., Jina, A.S., Kinney, P.L. et al. Extreme Air Pollution in Global Megacities. Curr Clim Change Rep 2, 15–27 (2016). https://doi.org/10.1007/s40641-016-0032-z

Martin, R. L. and T.W. Good (1991), Catalyzed oxidation of sulfur dioxide in solution: the iron-manganese synergism, Atmospheric Environment, 25A, 2395-2399, doi: 10.1016/0960-1686(91)90113-L.

Massad, R.-S., E. Nemitz, and M. A. Sutton (2010), Review and parameterization of bi-directional ammonia exchange between vegetation and the atmosphere, Atmos. Chem. Phys., 10, 10359-10386, doi: 10.5194/acp-10-10359-2010.

Mathur, R., Yu, S., Kang, D., & Schere, K. L. (2008). Assessment of the wintertime performance of developmental particulate matter forecasts with the Eta-Community Multiscale Air Quality modeling system. Journal of Geophysical Research, 113(D2), D02303. https://doi.org/10.1029/2007JD008580

Matthias, V., Jan A. Arndt, Armin Aulinger, Johannes Bieser, Hugo Denier van der Gon, Richard Kranenburg, Jeroen Kuenen, Daniel Neumann, George Pouliot & Markus Quante (2018) Modeling emissions for three-dimensional atmospheric chemistry transport models, Journal of the Air & Waste Management Association, 68:8, 763-800, DOI: 10.1080/10962247.2018.1424057

McKeen, S., Wilczak, J., Grell, G., Djalova, I., Peckham, S., Hsie, E.-Y., Gong, W., Bouchet, V., Ménard, S., Moffet, R., McHenry, J., McQueen, J., Tang, Y., Carmichael, G.R., Pagowski, M., Chan, A., Dye, t., Frost, G., Lee, P., Mathur, R.,

2005. Assessment of an ensemble of seven real-time ozone forecasts over eastern North America during the summer of 2004. J. Geophys. Res. 110, D21307. http://dx.doi.org/10.1029/2005JD005858.

McKeen, S., Chung, S.H., Wilczak, J., Grell, G., Djalalova, I., Peckham, S., Gong, W., Bouchet, V., Moffet, R., Tang, Y., Carmichael, G.R., Mathur, R., Yu, S., 2007. Evaluation of several PM2.5 forecast models using data collected during the ICARTT/NEAQS 2004 field study. J. Geophys. Res. 112, D10S20. http://dx.doi.org/10.1029/2006JD007608.

McKeen, S., et al., 2009. An evaluation of real-time air quality forecasts and their urban emissions over eastern Texas during the summer of 2006 Second Texas Air Quality Study field study. J. Geophys. Res. 114, D00F11. http://dx.doi.org/10.1029/2008JD011697.

Miller J, Safford H, Crimmins M, Thode A (2009) Quantitative evidence for increasing forest fire severity in the Sierra Nevada and Southern Cascade Mountains, California and Nevada, USA. Ecosystems 12:16–32

Mlawer, E. J., , Taubman S. J. , , Brown P. D. , , Iacono M. J. , , and Clough S. A. , 1997: Radiative transfer for inhomogeneous atmosphere: RTTM, a validated correlated-k model for the longwave. J. Geophys. Res., 102, 16 663–16 682, doi:10.1029/97JD00237.

Monin, A. S., & Obukhov, A. M. (1954). Basic laws of turbulent mixing in the surface layer of the atmosphere (in Russian). Contribution Geophysics Institute, Academy of Sciences USSR, 151, 163–187.

Myneni, R., Knyazikhin, Y. (2018). VIIRS/NPP Leaf Area Index/FPAR 8-Day L4 Global 500m SIN Grid V001 [Data set]. NASA EOSDIS Land Processes DAAC. Accessed 2021-02-22 from https://doi.org/10.5067/VIIRS/VNP15A2H.001

National Emissions Inventory (NEI). (2014). Retrieved February 26, 2020, from https://edap.epa.gov/public/extensions/nei_report_2014/dashboard.html#sector-db

National Emissions Inventory Collaborative (2019). 2016v1 Emissions Modeling Platform. Retrieved from http://views.cira.colostate.edu/wiki/wiki/10202.

Nemitz, E., Sutton, M. A., Schjoerring, J. K., Husted, S., & Wyers, G. P. (2000). Resistance modelling of ammonia exchange over oilseed rape. Agricultural and Forest Meteorology, 105(4), 405–425. https://doi.org/10.1016/S0168-1923(00)00206-9

Niinemets, Ü., Arneth, A., Kuhn, U., Monson, R. K., Peñuelas, J., and Staudt, M.: The emission factor of volatile isoprenoids: stress, acclimation, and developmental responses, Biogeosciences, 7, 2203–2223, doi:10.5194/bg-7-2203-2010, 2010.

O'Neill MS, , et al. Health, wealth, and air pollution: Advancing theory and methods. Environ Health Perspect. 2003; 111: 1861-1870

O'Neill, S. M., and Coauthors, 2009: Regional real-time smoke prediction systems. Wildland Fires and Air Pollution, A. Bytnerowicz et al., Eds., Developments in Environmental Science, Vol. 8, Elsevier, 499–534.

Otte, T. L. and Pleim, J. E.: The Meteorology-Chemistry Interface Processor (MCIP) for the CMAQ modeling system: updates through MCIPv3.4.1, Geosci. Model Dev., 3, 243–256, https://doi.org/10.5194/gmd-3-243-2010, 2010.

Otte, T. L., Pouliot, G., Pleim, J. E., Young, J. O., Schere, K. L., Wong, D. C., et al. (2005). Linking the Eta Model with the Community Multiscale Air Quality (CMAQ) Modeling System to Build a National Air Quality Forecasting System. Weather and Forecasting, 20(3), 367–384. https://doi.org/10.1175/WAF855.1

Pan, L., Kim, H., Lee, P., Saylor, R., Tang, Y., Tong, D., Baker, B., Kondragunta, S., Xu, C., Ruminski, M. G., Chen, W., McQueen, J., and Stajner, I.: Evaluating a fire smoke simulation algorithm in the National Air Quality Forecast Capability (NAQFC) by using multiple observation data sets during the Southeast Nexus (SENEX) field campaign, Geosci. Model Dev., 13, 2169–2184, https://doi.org/10.5194/gmd-13-2169-2020, 2020.

Pinder, R.W., Dennis, R.L., Bhave, P.V., 2008. Observable indicators of the sensitivity of PM2.5 nitrate to emission reductions: part I. Derivation of the adjusted gas ratio and applicability at regulatory-relevant time scales. Atmos. Environ. 42 (6), 1275e1286.

Pleim, J. E., 2007a: A combined local and nonlocal closure model for the atmospheric boundary layer. Part I: Model description and testing. J. Appl. Meteor. Climatol., 46, 1383–1395, doi:10.1175/JAM2539.1.

Pleim, J. E., 2007b: A combined local and nonlocal closure model for the atmospheric boundary layer. Part II: Application and evaluation in a mesoscale meteorological model. J. Appl. Meteor. Climatol., 46, 1396–1409, doi:10.1175/JAM2534.1.

Pleim, J., & Ran, L. (2011). Surface flux modeling for air quality applications. Atmosphere, 2(3), 271–302. https://doi.org/10.3390/atmos2030271.

Pleim, J. E., Bash, J. O., Walker, J. T., & Cooter, E. J. (2013). Development and evaluation of an ammonia bidirectional flux parameterization for air quality models. Journal of Geophysical Research: Atmospheres, 118, 3794–3806. https://doi.org/10.1002/jgrd.50262

Pleim, J. E., Ran, L., Appel, W., Shephard, M. W., & Cady-Pereira, K. (2019). New bidirectional ammonia flux model in an air quality model coupled with an agricultural model. Journal of Advances in Modeling Earth Systems, 11, 2934– 2957. https://doi.org/10.1029/2019MS001728

Powers, J. G., Klemp, J. B., Skamarock, W. C., Davis, C. A., Dudhia, J., Gill, D. O., et al. (2017). The weather research and forecasting model: Overview, system efforts, and future directions. Bulletin of the American Meteorological Society, 98(8), 1717–1737. https://doi.org/10.1175/BAMS-D-15-00308.1

Putman, W. M., and S.-J. Lin (2007). Finite-volume transport on various cubed-sphere grids, Journal of Computational Physics, 227, 1, 10, 55-78. https://doi.org/10.1016/j.jcp.2007.07.022

Pye, H. O. T., R. W. Pinder, I. Piletic, Y. Xie, S. L. Capps, Y.-H. Lin, J. D. Surratt, Z. Zhang, A. Gold, D. J. Luecken, W. T. Hutzell, M. Jaoui, J. H. Offenberg, T. E. Kleindienst, M. Lewandowski, and E. O. Edney, Epoxide pathways improve model predictions of isoprene markers and reveal key role of acidity in aerosol formation, Environmental Science & Technology, https://doi.org/10.1021/es402106h, 2013.

Pye, H. O. T., Murphy, B. N., Xu, L., Ng, N. L., Carlton, A. G., Guo, H., Weber, R., Vasilakos, P., Appel, K. W., Budisulistiorini, S. H., Surratt, J. D., Nenes, A., Hu, W., Jimenez, J. L., Isaacman-VanWertz, G., Misztal, P. K., and Goldstein, A. H.: On the implications of aerosol liquid water and phase separation for organic aerosol mass, Atmospheric Chemistry and Physics, 17, 343-369, https://doi.org/10.5194/acp-17-343-2017, 2017.

Ran, L., Cooter, E., Benson, V., & He, Q. (2011). Development of an agricultural fertilizer modeling system for bi-directional ammonia fluxes in the CMAQ model. In D. G. Steyn, & S. T. Castelli (Eds.), Air Pollution Modeling and its Application XXI (Chapter 36, (pp. 213–219). Dordrecht: Springer. https://doi.org/10.1007/978-94-007-1359-8_36

Ran, L., J. Pleim, R. Gilliam, F. S. Binkowski, C. Hogrefe, and L. Band (2016), Improved meteorology from an updated WRF/CMAQ modeling system with MODIS vegetation and albedo, J. Geophys. Res. Atmos., 121, 2393– 2415, doi:10.1002/2015JD024406.

Rogers et al., 1996 E. Rogers, T. Black, D. Deaven, G. DiMego, Q. Zhao, M. Baldwin, N. Junker, Y. Lin Changes to the operational "early" Eta Analysis/Forecast System at the National Centers for Environmental Prediction Weather and Forecasting, 11 (1996), pp. 391-413

Ruminski, M. and Kondragunta, S.: Monitoring fire and smoke emissions with the hazard mapping system – art. no. 64120B. in: Disaster Forewarning Diagnostic Methods and Management, edited by: Kogan, F., Habib, S., Hegde, V. S., and Matsuoka, M., 2006.

Ruminski, M., Simko, J., Kibler, J., Kondragunta, S., Draxler, R., Davidson, P., and Li, P.: Use of multiple satellite sensors in NOAA's operational near real-time fire and smoke detection and characterization program, in: Remote Sensing of Fire: Science and Application, edited by: Hao, W. M., 2008.

Sarwar, G., K. Fahey, S. Napelenok, S. Roselle, and R. Mathur (2011), Examining the impact of CMAQ model updates on aerosol sulfate predictions, the 10th Annual CMAS Models-3 User's Conference, October, Chapel Hill, NC.

Sarwar, G., B. Gantt, K. Foley, K. Fahey, T. L. Spero, D. Kang, R. Mathur, H. Foroutan, J. Xing, T. Sherwen, A. Saiz-Lopez (2019). Influence of bromine and iodine chemistry on annual, seasonal, diurnal, and background ozone: CMAQ simulations over the Northern Hemisphere. Atmospheric Environment. 213. 395-404. https://doi.org/10.1016/j.atmosenv.2019.06.020.

Schwede, D., G. A. Pouliot, and T. Pierce (2005), Changes to the Biogenic Emissions Inventory System Version 3 (BEIS3), In Proceedings of the 4th CMAS Models-3 Users' Conference, Chapel Hill, NC, 26–28 September 2005.

Schroeder, W., Ruminski, M., Csiszar, I., Giglio, L., Prins, E., Schmidt, C., and Morisette, J.: Validation analyses of an operational fire monitoring product: The Hazard Mapping System, Int. J. Remote Sens., 29, 6059–6066, https://doi.org/10.1080/01431160802235845, 2008.

Sillman, S., Logan, J. A. & Wofsy, S. C. The sensitivity of ozone to nitrogen oxides and hydrocarbons in regional ozone episodes. J. Geophys. Res. 95, 1837–1852 (1990).
Sillman, S. The use of NOy, H2O2, and HNO3 as indicators for ozone-NOx-hydrocarbon sensitivity in urban locations. J. Geophys. Res. Atmos. 100, 14175–14188 (1995).
Sillman, S., The relation between ozone, NOx and hydrocarbons in urban and polluted rural environments. Millenial Review series, Atmos. Environ., 33, 12, 1821-1845, 1999.

Skamarock, W. C., & Klemp, J. B. (2008). A time-split nonhydrostatic atmospheric model for weather research and forecasting applications. Journal of Computational Physics, 227(7), 3465–3485. https://doi.org/10.1016/j.jcp.2007.01.037

Skamarock, W. C., Klemp, J. B., Dudhia, J., Gill, D. O., Liu, Z., Berner, J., Huang, X. -yu. (2019). A Description of the Advanced Research WRF Model Version 4 (No. NCAR/TN-556+STR). doi:10.5065/1dfh-6p97

Sofiev, M., Ermakova, T., and Vankevich, R.: Evaluation of the smoke-injection height from wild-land fires using remote-sensing data, Atmos. Chem. Phys., 12, 1995–2006, https://doi.org/10.5194/acp-12-1995-2012, 2012.

Stajner, I., Davidson, P., Byun, D., McQueen, J., Draxler, R., Dickerson, P., & Meagher, J. (2011). US National Air Quality Forecast Capability: Expanding Coverage to Include Particulate Matter (pp. 379–384). Springer, Dordrecht. https://doi.org/10.1007/978-94-007-1359-8_64

Jian Sun, Joshua S. Fu, Kan Huang & Yang Gao (2015) Estimation of future PM2.5- and ozone-related mortality over the continental United States in a changing climate: An application of high-resolution dynamical downscaling technique, Journal of the Air & Waste Management Association, 65:5, 611-623, DOI: 10.1080/10962247.2015.1033068

Tang, Youhua & Lee, Pius & Tsidulko, Marina & Huang, Ho-Chun & Mcqueen, Jeffery & DiMego, Geoffrey & Emmons, Louisa & Pierce, Robert & Thompson, Anne & Lin, Hsin-Mu & Kang, Daiwen & Tong, Daniel & Yu, Shaocai & Mathur, Rohit & Pleim, Jonathan & Otte, Tanya & Pouliot, George & Young, Jeffrey & Schere, Kenneth & Stajner, Ivanka. (2009). The impact of chemical lateral boundary conditions on CMAQ predictions of tropospheric ozone

over the continental United States. Environmental Fluid Mechanics. 9. 43-58. 10.1007/s10652-008-9092-5.

Tang, Y., Tianfeng Chai, Li Pan, Pius Lee, Daniel Tong, Hyun-Cheol Kim & Weiwei Chen (2015) Using optimal interpolation to assimilate surface measurements and satellite AOD for ozone and PM2.5: A case study for July 2011, Journal of the Air & Waste Management Association, 65:10, 1206-1216, DOI: 10.1080/10962247.2015.1062439

Tang, Y., Bian, H., Tao, Z., Oman, L. D., Tong, D., Lee, P., Campbell, P. C., Baker, B., Lu, C.-H., Pan, L., Wang, J., McQueen, J., and Stajner, I.: Comparison of chemical lateral boundary conditions for air quality predictions over the contiguous United States during pollutant intrusion events, Atmos. Chem. Phys., 21, 2527–2550, https://doi.org/10.5194/acp-21-2527-2021, 2021.

Tang Y., P. C. Campbell, P. Lee, R. Saylor, F. Yang, B. Baker, D. Tong, A. Stein, F. Yang, J. Huang, H.-C. Huang, J. McQueen, I. Stajner, J. Sims, J. Tirado-Delgado, and Y. Jung (2022). Evaluation of the NAQFC Driven by the NOAA Global Forecast System Version 16: Comparison with the WRF-CMAQ Downscaling Method During the Summer 2019 FIREX-AQ Campaign, GMD, In Prep.

Tewari, M., Chen, F., Wang, W., Dudhia, J., LeMone, M. A., Mitchell, K., et al. (2004). Implementation and verification of the unified NOAH land surface model in the WRF model. Paper Presented at the 20th Conference on Weather Analysis and Forecasting/16th Conference on Numerical Weather Prediction, Seattle, WA.

Tong, D.Q., P. Lee, and R.D. Saylor (2012). New Direction: The need to develop process-based emission forecasting models, Atmospheric Environment, 47: 560-561

Tong, D. Q., Wang, J. X. L., Gill, T. E., Lei, H., and Wang, B. (2017), Intensified dust storm activity and Valley fever infection in the southwestern United States, Geophys. Res. Lett., 44, 4304– 4312, doi:10.1002/2017GL073524.

Troen, I. and L. Mahrt, 1986: A simple model of the atmospheric boundary layer: Sensitivity to surface evaporation. Bound.-Layer Meteor., 37 , 129–148.

US EPA Office of Research and Development. (2014, May 30). CMAQv5.0.2 (Version 5.0.2). Zenodo. http://doi.org/10.5281/zenodo.1079898

US EPA Office of Research and Development. (2019, December 19). CMAQ (Version 5.3.1). Zenodo. http://doi.org/10.5281/zenodo.3585898

Vukovich, J. M., and T. Pierce (2002). The Implementation of BEIS3 within the SMOKE modeling framework.

Weiss, A. and Norman, J.: Partitioning solar radiation into direct and diffuse, visible and nearinfrared components, Agr. Forest Meteorol., 34, 205–213, 1985.

Westerling AL, Hidalgo HG, Cayan DR, Swetnam TW (2006) Warming and earlier spring increase western US forest wildfire activity. Science 313:940–943.

Wilkins, J., G. Pouliot, T. Pierce, AND J. Beidler. Exploring the Vertical Distribution of Wildland Fire Smoke in CMAQ (2019 IEIC). 2019 International Emissions Inventory Conference, Dallas, Texas, July 28 - August 02, 2019.

Williams, J. R. (1995). The EPIC model. In V. P. Singh (Ed.), Computer models in watershed hydrology (Chapter 25, (pp. 909–1000). Littleton, CO: Water Resources Publications.

Williams, A. P., Cook, E. R., Smerdon, J. E., Cook, B. I., Abatzoglou, J. T., Bolles, K., Baek, S. H., Badger, A. M., Livneh, B. (2020). Large contribution from anthropogenic warming to an emerging North American megadrought. Science. 368, 314-318. DOI: 10.1126/science.aaz9600.

World Health Organization (WHO), 2006. Air Quality Guidelines. Global update 2005. Particulate matter, ozone, nitrogen dioxide and sulfur dioxide.

World Health Organization (WHO), 2010. WHO Guidelines for Indoor Air Quality: Selected Pollutants. World Health Organization, Regional Office for Europe Scherfigsvej 8, DK-2100 Copenhagen Ø, Denmark, ISBN 9789289002134.

Yang, F., Tallapragada, V., Kain, J. S., Wei, H., Yang, R., Yudin, V. A., Moorthi, S., Han, J., Hou, Y. T., Wang, J., Treadon, R., and Kleist, D. T. (2020). Model Upgrade Plan and Initial Results from a Prototype NCEP Global Forecast System Version 16. 2020 AMS Conference, Boston, MA. https://ams.confex.com/ams/2020Annual/webprogram/Paper362797.html

Yarwood, G., Rao S., Yocke M., and Whitten G., 2005: Updates to the carbon bond chemical mechanism: CB05. Final Rep. to the US EPA, RT-0400675. [Available online at http://www.camx.com/publ/pdfs/cb05_final_report_120805.pdf.]

Yarwood, G., G. Z. Whitten, and J. Jung (2010). Final Report. Development, Evaluation and Testing of Version 6 of the Carbon Bond Chemical Mechanism (CB6). ENVIRON International Corporation. 06-17477Y. September 22, 2010.

Zeka A, Zanobetti A, Schwartz J. Short term effects of particulate matter on cause specific mortality: effects of lags and modification by city characteristics. Occup Environ Med. 2006; 62: 718-725

Zhang, X., Kondragunta, S., Ram, J., Schmidt, C., & Huang, H.-C. (2012). Near-real-time global biomass burning emissions product from geostationary satellite constellation. Journal of Geophysical Research: Atmospheres, 117(D14). https://doi.org/10.1029/2012JD017459

Zhang, X., Kondragunta, S., & Roy, D. P. (2014). Interannual variation in biomass burning and fire seasonality derived from geostationary satellite data across the contiguous United States from 1995 to 2011. Journal of Geophysical Research: Biogeosciences, 119(6), 1147–1162. https://doi.org/10.1002/2013JG002518.

Zhang, Y., Vijayaraghavan, K., Wen, X.-Y., Snell, H.E., Jacobson, M.Z., 2009a. Probing into regional ozone and particulate matter pollution in the United States: 1. A 1 year CMAQ simulation and evaluation using surface and satellite data. J. Geophys. Res. 114, D22304.

Zhang, Y., Wen, X.-Y., Wang, K., Vijayaraghavan, K., Jacobson, M.Z., 2009b. Probing into regional ozone and particulate matter pollution in the United States: 2. An examination of formation mechanisms through a process analysis technique and sensitivity study. J. Geophys. Res. 114.

Zhang, Y., Bocquet, M., Mallet, V., Seigneur, C., and Baklanov, A. (2012a), Real-time air quality forecasting, part I: History, techniques, and current status. Atmospheric Environment. 60, 632-655.

Zhang, Y., Bocquet, M., Mallet, V., Seigneur, C., and Baklanov, A. (2012b), Real-time air quality forecasting, part II: State of the science, current research needs, and future prospects. Atmospheric Environment. 60, 656-676.

Zhang, Y., West, J. J., Mathur, R., Xing, J., Hogrefe, C., Roselle, S. J., Bash, J. O., Pleim, J. E., Gan, C.-M., and Wong, D. C.: Long-term trends in the ambient PM2.5- and O3-related mortality burdens in the United States under emission reductions from 1990 to 2010, Atmos. Chem. Phys., 18, 15003–15016, https://doi.org/10.5194/acp-18-15003-2018, 2018.

Zhao, H.; Zheng, Y.; Li, T. Air Quality and Control Measures Evaluation during the 2014 Youth Olympic Games in Nanjing and its Surrounding Cities. Atmosphere 2017, 8, 100.

Zhou, L., S. Lin, J. Chen, L.M. Harris, X. Chen, and S.L. Rees, 2019: Toward Convective-Scale Prediction within the Next Generation Global Prediction System. Bull. Amer. Meteor. Soc., 100, 1225–1243, https://doi.org/10.1175/BAMS-D-17-0246.1

Zhou, T.; Sun, J.; Yu, H. Temporal and Spatial Patterns of China's Main Air Pollutants: Years 2014 and 2015. Atmosphere 2017, 8, 137.